

Relationships between the Stellar, Gaseous, and Star Formation Disks in LITTLE THINGS Dwarf Irregular Galaxies: Indirect Evidence for Substantial Fractions of Dark Molecular Gas

Deidre A. Hunter¹, Bruce G. Elmegreen², Esther Goldberger^{1,3}, Hannah Taylor^{1,4}, Anton I. Ermakov^{1,4,5}, Kimberly A. Herrmann⁶, Se-Heon Oh⁷, Bradley Malko^{1,8}, Brian Barandi^{1,8}, Ryan Jundt^{1,8}

ABSTRACT

The stellar, gaseous and young stellar disks in the LITTLE THINGS sample of nearby dIrrs are fitted with functions to search for correlations between the parameters. We find that the H I radial profiles are generally flatter in the center and fall faster in the outer regions than the V -band profiles, while young stars are more centrally concentrated, especially if the H I is more centrally flat. This pattern suggests that the H I is turning into molecules in the center and the molecular clouds are forming stars and FUV. A model that assumes the molecular surface density is proportional to the total gas surface density to a power of 1.5 or 2, in analogy with the Kennicutt-Schmidt relation, reproduces the relationship between the ratio of the visible to the H I scale length and the H I Sersic index. The molecular fraction is estimated as a function of radius for each

¹Lowell Observatory, 1400 West Mars Hill Road, Flagstaff, AZ 86001, USA

²IBM T. J. Watson Research Center, PO Box 218, Yorktown Heights, New York

³Department of Physics, Massachusetts Institute of Technology, 77 Massachusetts Ave., 54-918, Cambridge, MA 02142, USA

⁴Department of Earth, Atmospheric, and Planetary Sciences, Massachusetts Institute of Technology, 77 Massachusetts Avenue, Cambridge, MA 02139-4307, USA

⁵Current affiliation Earth and Planetary Science Department, University of California-Berkeley, Berkeley, CA 94709, USA

⁶Department of Physics, Pennsylvania State University Mont Alto, 1 Campus Drive, Mont Alto, PA 17237, USA

⁷Department of Physics and Astronomy, Sejong University, 209 Neungdong-ro, Gwangjin-gu, Seoul, Republic of Korea

⁸Department of Astronomy and Planetary Sciences, Northern Arizona University, Flagstaff, AZ 86001, USA

galaxy by converting the FUV to a molecular surface density using conventional calibrations. The average molecular fraction inside $3R_D$ is $23 \pm 17\%$. However, the break in the stellar surface brightness profile has no unified tracer related to star formation.

Subject headings: galaxies: irregular — galaxies: star formation — galaxies: ISM — galaxies: structure

1. Introduction

Dwarf irregular (dIrr) galaxies contain stellar populations and most also have on-going star formation. Yet, their atomic gas surface densities, even in their centers, are low compared to those in the central regions of spirals. In fact the gas surface densities in dIrr galaxies and the outer parts of spirals are lower than the threshold necessary for gravitational instabilities to make clouds that can then go on to make stars as is believed to happen in the central regions of spirals (Toomre 1964; Kennicutt 1989; Hunter et al. 1998; Bigiel et al. 2010; Barnes et al. 2012; Kennicutt 1989; Elmegreen & Hunter 2015a). Furthermore, dIrr galaxies have extended stellar disks that have been traced up to 12 disk scale lengths, R_D , (e.g. Saha et al. 2010; Sanna et al. 2010; Hunter et al. 2011; Bellazzini et al. 2014), and young stars are found in the far outer parts of dIrr and spiral galaxies (Thilker et al. 2005; Hunter et al. 2016). Thus, star formation appears to be taking place in extreme environments of sub-threshold gas densities. In addition, star formation appears to have proceeded “outside-in” in dIrrs (Zhang et al. 2012; Gallart et al. 2008; Meschin et al. 2014; Pan et al. 2015). By contrast, spiral stellar disks are observed to grow from “inside-out” (e.g., Williams et al. 2009). The cause of this difference in disk formation is also not understood.

H I gas extends well beyond the bright stellar part of the galaxy in both spirals (e.g. Warmels 1986; Broeils 1992; Rao & Briggs 1993; van der Hulst et al. 1993) and dwarfs (e.g. Hunter & Gallagher 1985; Meurer et al. 1996) with an unusual concentration of H I towards the centers in Blue Compact Dwarfs (e.g. van Zee et al. 1998; Simpson & Gottesman 2000). The ratio of the mass in stars to mass in atomic gas drops steadily with radius in dIrr galaxies (see, for example, Figure 4 in Hunter 2008). Dwarfs are usually gas dominated even in the centers, but become more so with radius. This implies a steady decrease in the efficiency of conversion of atomic gas into stars with distance from the center of the galaxy (see, for example, Leroy et al. 2008).

Since stars form from dense gas clouds that presumably form from the general atomic interstellar medium (ISM) in a galaxy, we expect there to be a relationship between gas

density and cloud-forming instabilities (e.g. Toomre 1964) and, hence, between gas density and the formation of stars (Goldreich & Lynden-Bell 1965). Yet, the apparent wide variety of ways the gas surface density falls off with radius in dIrr galaxies is striking. Some profiles are relatively flat, some drop precipitously, and others decrease steadily. This variety seems to be far greater than the uniformly exponential surface brightness profiles seen in the stellar disks of most dIrr systems. Empirical relationships show a general correspondence between gas and star formation (see, for example, Bigiel et al. 2008, 2010). Yet, the physical connection between large-scale gas distributions and the formation of new stars is still illusive and empirically a large range in star formation rates (SFRs) can be found at a given surface density of the atomic gas. What then is the role of the gas in determining the nature of the stellar disk? This question is particularly compelling in outer stellar disks where we see young stars but the gas densities are especially low.

However, there is a further complication in understanding how the gas and stars are related: most stellar disk surface brightnesses do not drop off with radius at a single rate. Most, both spiral and dIrr, show a break in their stellar exponential disks. The stellar surface brightness profile drops off exponentially, and then at the break radius R_{Br} it either drops more steeply (Type II break, Freeman 1970) or drops less steeply (the less common Type III break, which could be the signature of a lopsided disk, Erwin et al. 2005; Watkins et al. 2019). A Type I disk has no break (Freeman 1970). In spiral galaxies, the break is not as apparent in the mass surface density profiles as in the stellar surface brightness profiles (Bakos et al. 2008) and this could be related to the potential for spiral arms to scatter inner disk stars to the outer regions (Bournaud et al. 2007; Roškar et al. 2008). On the other hand, scattering is less effective in dIrr galaxies (Struck & Elmegreen 2017), which do not have spiral arms, and the break is also seen in the stellar mass surface density profiles of these galaxies (Herrmann et al. 2016). Star formation processes could also vary with radius, including the ability to form molecules, which should be more prevalent in the inner regions of dwarfs than the outer regions (e.g., Hunter et al. 2019a), which could potentially lead to a break in the stellar profile. Alternatively, Andersen & Burkert (2000) suggest that self-regulated evolution within a confining dark halo leads to exponential density profiles that are somewhat flatter in the central regions.

To explore the factors at play in determining the structure of the stellar disk in dwarf galaxies, we have parameterized the radial profiles of H I mass surface densities, H I rotation, stellar surface brightness, and star formation activities of a sample of nearby dwarf galaxies that are part of LITTLE THINGS (Local Irregulars That Trace Luminosity Extremes, The H I Nearby Galaxy Survey; Hunter et al. 2012). We compare the characteristics of the gas and star formation activity with those of the stellar disk, looking for correlations that could be clues to processes that shape the stellar disk. We also look for hidden H₂ in the form of

missing gas connected with star formation.

2. Data

LITTLE THINGS⁹ is a multi-wavelength survey aimed at determining what drives star formation in dwarf galaxies (Hunter et al. 2012). The LITTLE THINGS sample includes 37 dIrr galaxies and 4 Blue Compact Dwarf (BCD) galaxies, and is centered around H I-emission data obtained with the National Science Foundation’s Karl G. Jansky Very Large Array (VLA¹⁰). The H I-line data are characterized by high sensitivity (≤ 1.1 mJy beam⁻¹ per channel), high spectral resolution (1.3 or 2.6 km s⁻¹), and high angular resolution (typically 6”). The LITTLE THINGS sample contains dwarf galaxies that are relatively nearby (≤ 10.3 Mpc; 6” is ≤ 300 pc), contain gas so they have the potential for star formation, and are not companions to larger galaxies. The sample was also chosen to cover a large range in dwarf galactic properties such as SFR and absolute magnitude.

The LITTLE THINGS ancillary data include far-ultraviolet (FUV) images obtained with the NASA *Galaxy Evolution Explorer* satellite (*GALEX*¹¹; Martin et al. 2005) to trace star formation over the past 200 Myr. These data give us integrated SFRs (Hunter et al. 2010) and the radius at which we found the furthest out FUV knot R_{FUVknot} in each galaxy (Hunter et al. 2016). So that galaxies can be compared, the SFRs are normalized to the area within one disk scale length and are, technically, SFR surface densities, although star formation is usually found beyond $1R_{\text{D}}$. LITTLE THINGS H α images give us the SFR over the past 10 Myr and the radius of the furthest out H II region $R_{\text{H}\alpha}$ (Hunter & Elmegreen 2004). Surface photometry of *UBVJHK* images was used by Herrmann et al. (2013) and Herrmann et al. (2016) to investigate the breaks in stellar surface brightness profiles, the radius at which there is a sudden change in the slope of the exponential decline. Here we use the break radius R_{Br} and disk scale length R_{D} determined from the *V*-band image. We also use the integrated galactic luminosities from Hunter & Elmegreen (2006).

⁹The original VLA survey was funded in part by the National Science Foundation through grants AST-0707563, AST-0707426, AST-0707468, and AST-0707835 to US-based LITTLE THINGS team members and supported with generous technical and logistical support from the National Radio Astronomy Observatory.

¹⁰The VLA is a facility of the National Radio Astronomy Observatory. The National Radio Astronomy Observatory is a facility of the National Science Foundation operated under cooperative agreement by Associated Universities, Inc.

¹¹*GALEX* was operated for NASA by the California Institute of Technology under NASA contract NAS5-98034.

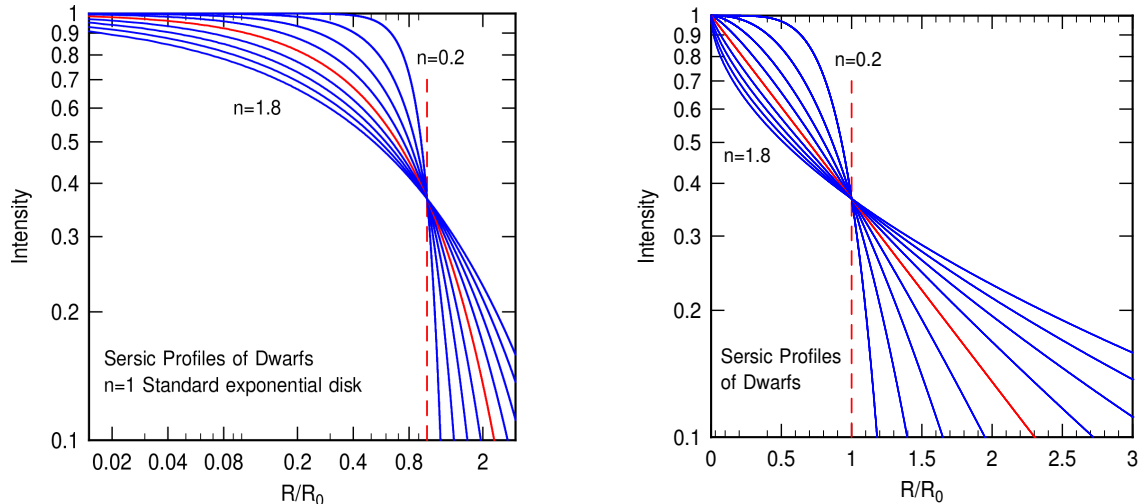


Fig. 1.— Family of Sersic profiles covering the H I fall off in the LITTLE THINGS dwarf galaxy sample plotted against $\log R$ (*left*) and linear R (*right*). An $n = 1$ curve (red solid line) is a standard exponential disk, and $n = 4$ would be an ellipsoidal system (de Vaucouleurs & Capaccioli 1979). The vertical dashed line marks $R/R_0 = 1$.

The galaxy sample and characteristics that we use here are given in Table 1. In some plots, we distinguish between those dIrrs that are classified as Magellanic irregulars (dIm) and those that are classified as BCDs (Haro 29, Haro 36, Mrk 178, VII Zw403).

3. Radial Profiles

3.1. H I Surface Density

The H I surface density profiles of the LITTLE THINGS dwarfs are described and shown by Hunter et al. (2012). We performed a multi-variable least squares fit of a Sersic (1982) profile to the gas distributions measured from velocity-integrated ROBUST-weighted maps. The Sersic profile, as used here, is

$$I(R) = I_0 e^{-(R/R_0)^{1/n}}. \quad (1)$$

For our situation, this can be re-written as

$$\log \Sigma_{\text{HI}}(R) = \log \Sigma_{\text{HI}}^0 - 0.434(R/R_{0,\text{HI}})^{1/n_{\text{HI}}}, \quad (2)$$

so that the H I surface density profiles are defined by three parameters: $\log \Sigma_{\text{HI}}^0$, the logarithm of the extrapolated central surface gas density in units of $M_\odot \text{ pc}^{-2}$; $R_{0,\text{HI}}$, a characteristic

Table 1. The Galaxy Sample

Galaxy	D ^a (Mpc)	M _V	R _{Hα} ^b (kpc)	R _{FUVknot} ^c (kpc)	R _D ^d (kpc)	R _{Br} ^e (kpc)	log SFR _D ^{FUVf} (M _⊙ yr ⁻¹ kpc ⁻²)	C ₃₁ ^g	log FUV _{1R_D} /FUV _{1–3R_D} ^h
CVnIdwA	3.6 ± 0.08	-12.37 ± 0.09	0.69	0.49±0.03	0.25±0.12	0.56±0.49	-1.77 ± 0.04	2.53	-0.14 ± 0.06
DDO 43	7.8 ± 0.8	-15.06 ± 0.22	2.36	1.93±0.08	0.87±0.10	1.46±0.53	-2.20 ± 0.04	...	0.60 ± 0.06
DDO 46	6.1 ± 0.4	-14.67 ± 0.16	1.51	3.02±0.06	1.13±0.05	1.27±0.18	-2.45 ± 0.04	...	0.92 ± 0.06
DDO 47	5.2 ± 0.6	-15.46 ± 0.24	5.58	5.58±0.05	1.34±0.05	...	-2.38 ± 0.04	...	0.54 ± 0.06
DDO 50	3.4 ± 0.05	-16.61 ± 0.03	...	4.86±0.03	1.48±0.06	2.65±0.27	-1.81 ± 0.04	2.45	0.51 ± 0.06
DDO 52	10.3 ± 0.8	-15.45 ± 0.17	3.69	3.39±0.10	1.26±0.04	2.80±1.35	-2.53 ± 0.04	2.68	0.42 ± 0.06
DDO 53	3.6 ± 0.05	-13.84 ± 0.03	1.25	1.19±0.03	0.47±0.01	0.62±0.09	-1.96 ± 0.04	2.10	0.68 ± 0.06
DDO 63	3.9 ± 0.05	-14.78 ± 0.03	2.26	2.89±0.04	0.68±0.01	1.31±0.10	-2.05 ± 0.04	2.29	0.12 ± 0.06
DDO 69	0.8 ± 0.04	-11.67 ± 0.11	0.76	0.76±0.01	0.19±0.01	0.27±0.05	-2.22 ± 0.04	2.36	0.28 ± 0.06
DDO 70	1.3 ± 0.07	-14.10 ± 0.12	1.23	1.34±0.01	0.44±0.01	0.13±0.07	-2.17 ± 0.04	2.77	1.03 ± 0.06
DDO 75	1.3 ± 0.05	-13.91 ± 0.08	1.17	1.38±0.01	0.18±0.01	0.71±0.08	-0.99 ± 0.04	2.03	-0.12 ± 0.06
DDO 87	7.7 ± 0.5	-14.98 ± 0.15	3.18	4.23±0.07	1.21±0.02	0.99±0.11	-2.61 ± 0.04	2.69	0.22 ± 0.06
DDO 101	6.4 ± 0.5	-15.01 ± 0.16	1.23	1.23±0.06	0.97±0.06	1.16±0.11	-2.84 ± 0.04	2.52	0.75 ± 0.06
DDO 126	4.9 ± 0.5	-14.85 ± 0.24	2.84	3.37±0.05	0.84±0.13	0.60±0.05	-2.18 ± 0.04	2.58	0.57 ± 0.06
DDO 133	3.5 ± 0.2	-14.75 ± 0.16	2.60	2.20±0.03	1.22±0.04	2.25±0.24	-2.60 ± 0.04	2.54	0.61 ± 0.06
DDO 154	3.7 ± 0.3	-14.19 ± 0.16	1.73	2.65±0.04	0.48±0.02	0.62±0.09	-1.77 ± 0.04	2.47	0.32 ± 0.06
DDO 155	2.2 ± 0.4	-12.53 ± 0.36	0.67	...	0.15±0.01	0.20±0.04	...	3.06	...
DDO 165	4.6 ± 0.4	-15.60 ± 0.19	3.16	...	2.24±0.08	1.46±0.08	...	2.30	...
DDO 167	4.2 ± 0.5	-12.98 ± 0.25	0.81	0.70±0.04	0.22±0.01	0.56±0.11	-1.59 ± 0.04	...	0.03 ± 0.06
DDO 168	4.3 ± 0.5	-15.72 ± 0.25	2.24	2.25±0.04	0.83±0.01	0.72±0.07	-2.06 ± 0.04	2.64	0.55 ± 0.06
DDO 187	2.2 ± 0.07	-12.68 ± 0.07	0.30	0.42±0.02	0.37±0.06	0.28±0.05	-2.60 ± 0.04	2.51	1.39 ± 0.06
DDO 210	0.9 ± 0.04	-10.88 ± 0.10	...	0.29±0.01	0.16±0.01	...	-2.66 ± 0.04	2.63	0.87 ± 0.06
DDO 216	1.1 ± 0.05	-13.72 ± 0.10	0.42	0.59±0.01	0.52±0.01	1.77±0.45	-3.17 ± 0.04	2.25	1.35 ± 0.06
F564-V3	8.7 ± 0.7	-13.97 ± 0.18	...	1.24±0.08	0.63±0.09	0.73±0.40	-2.94 ± 0.04	...	0.60 ± 0.06
IC 10	0.7 ± 0.05	-16.34 ± 0.16	0.39±0.01	0.30±0.04
IC 1613	0.7 ± 0.05	-14.60 ± 0.16	...	1.77±0.01	0.53±0.02	0.71±0.12	-1.97 ± 0.04	2.64	0.26 ± 0.06
LGS 3	0.7 ± 0.08	-9.74 ± 0.25	...	0.32±0.01	0.16±0.01	0.27±0.08	-3.75 ± 0.04	2.04	0.69 ± 0.06
M81dwA	3.6 ± 0.2	-11.73 ± 0.13	...	0.71±0.03	0.27±0.00	0.38±0.03	-2.30 ± 0.04	2.02	0.10 ± 0.06
NGC 1569	3.4 ± 0.2	-18.24 ± 0.13	...	1.14±0.03	0.46±0.02	0.85±0.24	-0.32 ± 0.04	3.13	1.41 ± 0.06
NGC 2366	3.4 ± 0.3	-16.79 ± 0.20	5.58	6.79±0.03	1.91±0.25	2.57±0.80	-2.04 ± 0.04	2.70	1.01 ± 0.06
NGC 3738	4.9 ± 0.5	-17.12 ± 0.24	1.48	1.21±0.05	0.77±0.01	1.16±0.20	-1.52 ± 0.04	2.95	1.76 ± 0.06
NGC 4163	2.9 ± 0.04	-14.45 ± 0.03	0.88	0.47±0.03	0.32±0.00	0.71±0.48	-1.89 ± 0.04	2.62	1.36 ± 0.06
NGC 4214	3.0 ± 0.05	-17.63 ± 0.04	...	5.46±0.03	0.75±0.01	0.83±0.14	-1.11 ± 0.04	3.09	0.96 ± 0.06
Sag DIG	1.1 ± 0.07	-12.46 ± 0.14	0.51	0.65±0.01	0.32±0.05	0.57±0.14	-2.40 ± 0.04	...	1.04 ± 0.06
UGC 8508	2.6 ± 0.1	-13.59 ± 0.13	0.79	...	0.23±0.01	0.41±0.06	...	2.49	...
WLM	1.0 ± 0.07	-14.39 ± 0.15	1.24	2.06±0.01	1.18±0.24	0.83±0.16	-2.78 ± 0.04	2.31	1.69 ± 0.06
Haro 29	5.8 ± 0.3	-14.62 ± 0.11	0.96	0.86±0.06	0.33±0.00	1.15±0.26	-1.21 ± 0.04	5.29	0.86 ± 0.06
Haro 36	9.3 ± 0.6	-15.91 ± 0.15	1.06	1.79±0.09	1.01±0.00	1.16±0.13	-1.88 ± 0.04	...	1.56 ± 0.06
Mrk 178	3.9 ± 0.5	-14.12 ± 0.26	1.17	1.45±0.04	0.19±0.00	0.38±0.00	-1.17 ± 0.04	2.78	0.18 ± 0.06
VIIZw403	4.4 ± 0.07	-14.27 ± 0.04	1.27	0.33±0.04	0.53±0.02	1.02±0.29	-1.80 ± 0.04	2.45	1.23 ± 0.06

^aDistance to the galaxy. References are given by Hunter et al. (2012). Uncertainty in the distance is folded into the uncertainty of M_V.

^bRadius of furthest out detected H II region R_{H α} in each galaxy from Hunter & Elmegreen (2004). Galaxies without H II regions or with H II regions extending beyond the area imaged do not have R_{H α} .

^cRadius of furthest out detected FUV knot R_{FUVknot} in each galaxy from Hunter et al. (2016). Galaxies without GALEX images have no value for this radius.

^dDisk scale length R_D determined from the V-band image surface photometry from Herrmann et al. (2013). In the case of galaxies with breaks in their surface brightness profiles, we have chosen the scale length that describes the primary underlying stellar disk.

^eBreak radius R_{Br} where the V-band surface brightness profile changes slope given by Herrmann et al. (2013). Galaxies without R_{Br} do not have breaks in their profiles.

^fSFR measured from the integrated FUV luminosity and normalized to the area within one R_D from Hunter et al. (2010). The normalization is independent of the radial extent of the FUV emission in a galaxy. We assume an uncertainty of 10%, which is greater than the photometric uncertainty.

^gA measure of the central concentration of stars - ratio of the radii that encompass 75% and 25% of the total stellar mass, from Zhang et al. (2012). A larger ratio means the stars are more centrally concentrated.

^hRatio of the FUV emission within the inner disk scale length R_D and the FUV emission in the annulus from radius 1R_D to 3R_D. A larger ratio means the FUV emission, and hence star formation, is centrally concentrated. We assume an uncertainty of 10% in both the numerator and the denominator.

radius; and n_{HI} , an index that controls the curvature of the profile. n is 4 for a de Vaucouleurs’ $R^{1/4}$ profile (for example, de Vaucouleurs & Capaccioli 1979) that is often used to describe elliptical galaxy stellar surface brightness profiles, and n is 1 for an exponential disk. Values of n_{HI} for our sample range between 0.2 and 1, with only two values larger than 1 (specifically, 1.29 for NGC 3738 and 1.65 for NGC 1569). The family of Sersic profiles demonstrated by LITTLE THINGS dIrr galaxies is shown in Figure 1, the HI profiles with the Sersic fits superposed are shown in Figure 2, and the fit parameters for each galaxy are given in Table 2.

We have compared the central measured HI surface mass density to $\log \Sigma_{HI}^0$ from the Sersic fit relative to the uncertainties in the two quantities. The uncertainty for the central point in the observed surface density profile was determined from the channel rms given by Hunter et al. (2012), the typical FWHM of the line profile in channels, and the area of the moment 0 map that was integrated. The uncertainty in the observed surface mass density was combined in quadrature with that for $\log \Sigma_{HI}^0$ from the Sersic fit. Only two galaxies, M81dwA and IC 1613, have a difference in the central mass densities that is greater than 3σ . One can see why these galaxies stand out: they have depressions in their centers.

We tried other representations in addition to the Sersic profile. In particular, we used a power law plus exponential

$$\Sigma_{HI}(R) = \frac{S}{R^A} \exp(-R^n) \quad (3)$$

where parameters of the fit are S , A , and n , and a disk galaxy fit from Wang et al. (2014)

$$\Sigma_{HI}(R) = \frac{I_1 \exp(-R/R_s)}{1 + I_2 \exp(-R/R_c)} \quad (4)$$

where fitting parameters are I_1 , I_2 , R_s , and R_c . The power law plus exponential did not fit the LITTLE THINGS data well. The Wang et al. (2014) fit was reasonable for 32 of the 40 galaxies, but generally the Sersic fit worked best overall and that is what we use here.

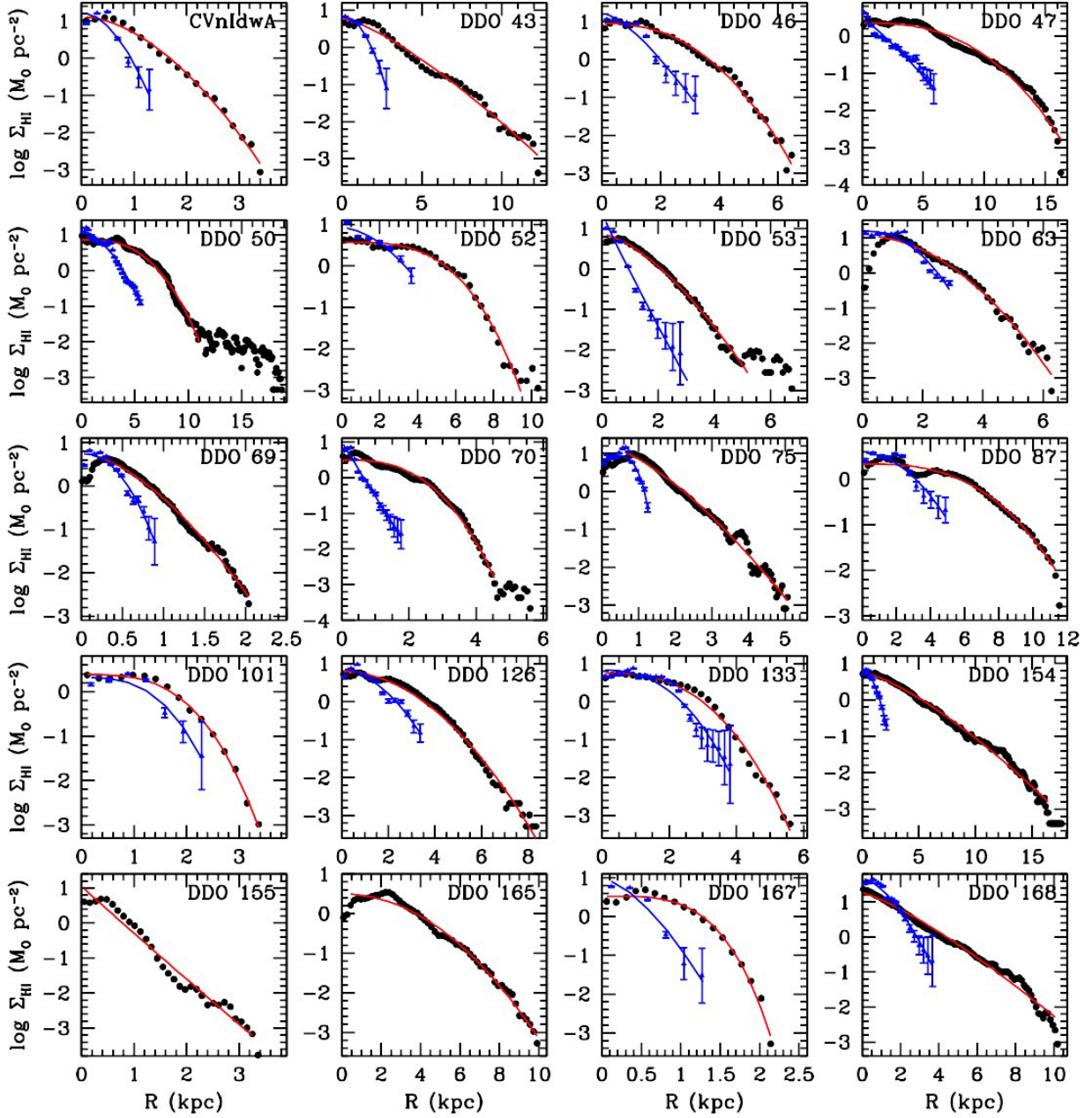
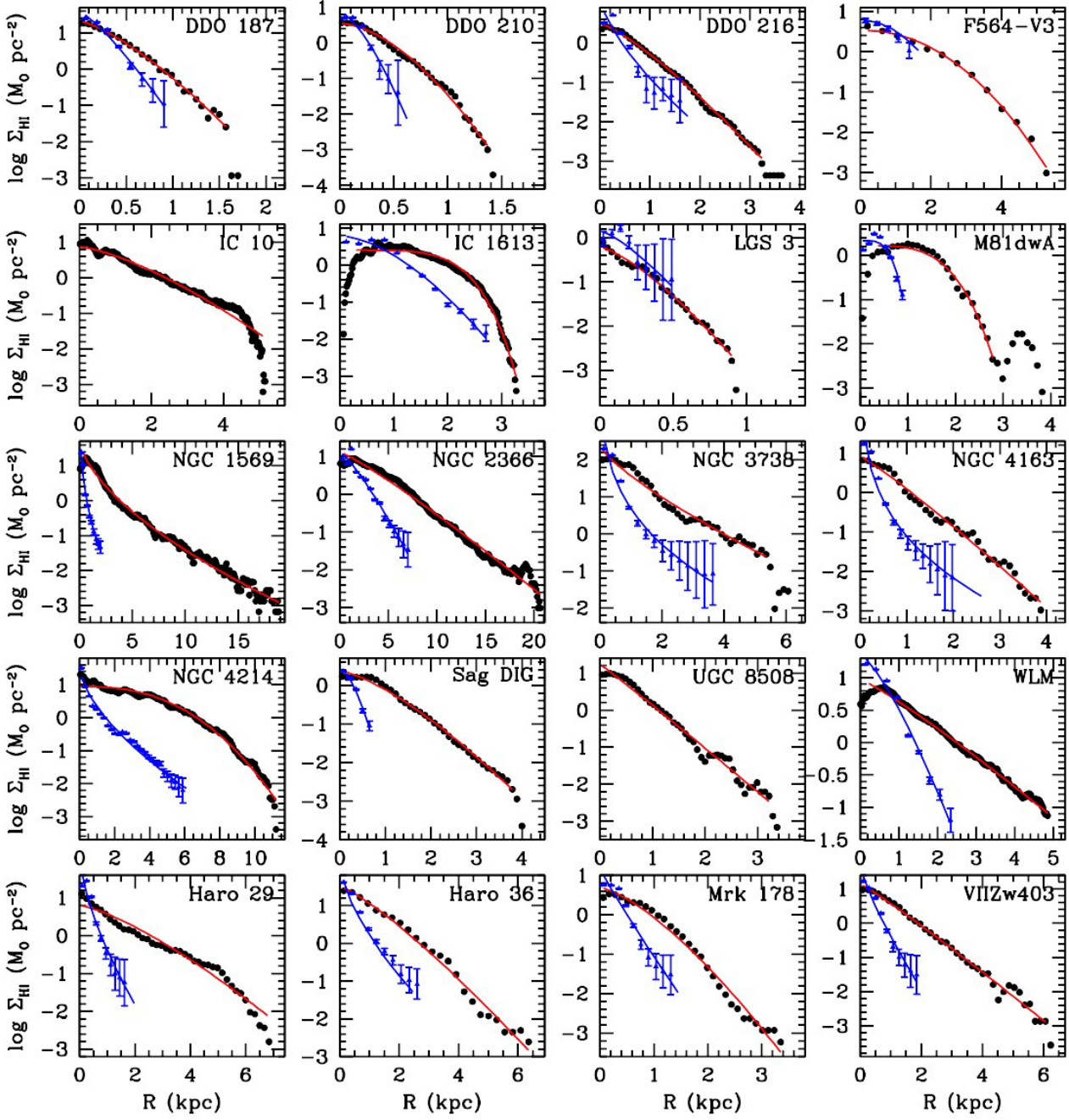


Fig. 2.— HI surface density profiles from Hunter et al. (2012). The red lines are the Sersic fits to the HI profiles. The blue triangles are FUV surface brightness profiles plotted with the same logarithmic interval as for the HI (Hunter et al. 2010; Zhang et al. 2012). Blue curves are Sersic fits to the FUV. DDO 155, DDO 165, IC 10, and UGC 8508 do not have FUV data.



3.2. FUV Luminosity

We have examined the SFR interior to R_{Br} compared to that exterior to the break. We used FUV as a tracer of the SFR because dust absorption is usually small in dIrr galaxies. We normalized the interior and exterior FUV luminosities in two ways: 1) relative to the area over which the FUV has been integrated, and 2) relative to the V -band luminosity in the same region. Normalizing to the V -band luminosity is comparable to normalizing the flux from young stars to that from older stellar populations. We used the *GALEX* FUV and V -band surface photometry for the LITTLE THINGS dwarfs. The effective wavelength of the FUV filter was 1516 Å and the resolution was 4.0". The FUV ratios are given in Table 3.

In order to compare this measurement of the dwarfs with those of spiral galaxies also with breaks in their surface brightness profiles, we used galaxies that are part of the *GALEX* Nearby Galaxy Survey (NGS) (Gil de Paz et al. 2007), which has obtained *GALEX* images of a wide range of spirals. Using the Lowell Observatory Hall 1.1 m telescope in January 2014, we obtained deep V -band images of 8 of the spirals in the NGS list. Galaxies were chosen to be not too edge on, observable from Flagstaff in January, and small enough for the field of view of the detector we used ($19' \times 19'$). In addition the galaxies were selected to cover the range of morphological type Sa, Sb, Sc, and Sd. Ultimately three of these galaxies were discarded, two because they did not have FUV images and one because it did not show a break in the V -band surface brightness profile. This left a sample of 5: one each of Sb, Sc, and Sd classifications, and two Sa galaxies. A sample of 5 is too small for characterizing either the mean or the dispersion in spiral galaxies of the SFR ratio parameter discussed here, especially as a function of spiral type, but we include these observations as a hint at the properties of spiral galaxies compared to those of the dIrr galaxies. In the Appendix we present the FUV and V surface photometry and their derived properties of these 5 spirals.

Table 2. Sersic Fit Parameters and Radii for H I

Galaxy	$\log \Sigma_{\text{HI}}^0$ ($M_{\odot} \text{ pc}^{-2}$)	$R_{0,\text{HI}}$ (kpc)	n_{HI}	$R_{50,\text{HI}}^{\text{a}}$ (kpc)	$(R_{50}/R_{90})_{\text{HI}}^{\text{a}}$
CVnIdwA	1.13±0.06	0.99±0.06	0.56±0.03	0.77±0.02	0.50±0.05
DDO 43	0.78±0.07	2.44±0.24	0.75±0.04	2.38±0.08	0.42±0.06
DDO 46	0.95±0.04	2.63±0.10	0.42±0.02	1.83±0.06	0.52±0.05
DDO 47	0.35±0.04	7.71±0.29	0.38±0.02	5.03±0.12	0.52±0.05
DDO 50	0.86±0.02	5.67±0.09	0.35±0.01	4.12±0.12	0.58±0.04
DDO 52	0.57±0.04	5.03±0.14	0.30±0.01	3.67±0.07	0.63±0.04
DDO 53	0.86±0.05	1.36±0.08	0.65±0.03	1.35±0.04	0.52±0.05
DDO 63	1.06±0.07	2.07±0.13	0.50±0.03	1.65±0.05	0.52±0.04
DDO 69	0.75±0.03	0.58±0.02	0.62±0.02	0.56±0.02	0.54±0.05
DDO 70	0.49±0.02	2.20±0.05	0.36±0.01	1.54±0.05	0.56±0.04
DDO 75	1.23±0.07	1.10±0.08	0.68±0.03	1.20±0.03	0.53±0.06
DDO 87	0.33±0.02	6.26±0.14	0.35±0.01	4.65±0.12	0.62±0.05
DDO 101	0.39±0.03	1.76±0.05	0.31±0.01	1.20±0.03	0.63±0.05
DDO 126	0.80±0.04	2.59±0.10	0.50±0.02	2.32±0.06	0.58±0.04
DDO 133	0.76±0.05	2.44±0.09	0.37±0.02	1.92±0.05	0.63±0.04
DDO 154	0.74±0.03	3.54±0.13	0.73±0.02	3.64±0.12	0.46±0.06
DDO 155	1.06±0.17	0.31±0.08	1.02±0.10	0.57±0.01	0.52±0.05
DDO 165	0.50±0.04	3.52±0.13	0.49±0.02	2.68±0.06	0.54±0.06
DDO 167	0.53±0.05	1.21±0.04	0.27±0.02	0.74±0.02	0.60±0.04
DDO 168	1.25±0.05	1.91±0.13	0.79±0.03	2.09±0.08	0.41±0.05
DDO 187	1.31±0.05	0.39±0.03	0.73±0.03	0.43±0.01	0.48±0.05
DDO 210	0.55±0.04	0.41±0.02	0.59±0.02	0.34±0.01	0.46±0.05
DDO 216	0.49±0.03	0.63±0.03	0.80±0.02	0.73±0.03	0.46±0.05
F564-V3	0.54±0.05	2.01±0.11	0.47±0.03	1.54±0.06	0.54±0.05
IC 10	0.86±0.03	1.47±0.08	0.71±0.03	1.48±0.06	0.44±0.05
IC 1613	0.40±0.01	2.18±0.02	0.20±0.00	1.36±0.03	0.62±0.04
LGS 3	-0.21±0.04	0.25±0.02	0.74±0.04	0.29±0.01	0.52±0.05
M81dwA	0.22±0.04	1.75±0.05	0.26±0.02	1.22±0.03	0.67±0.05
NGC 1569	1.79±0.09	0.37±0.06	1.65±0.06	1.92±0.08	0.30±0.06
NGC 2366	1.12±0.04	3.04±0.17	0.89±0.02	4.43±0.14	0.51±0.06
NGC 3738	2.39±0.12	0.44±0.12	1.29±0.12	1.09±0.04	0.36±0.06
NGC 4163	0.92±0.08	0.56±0.07	0.90±0.05	0.68±0.02	0.37±0.05
NGC 4214	0.95±0.02	4.89±0.11	0.40±0.01	3.74±0.10	0.58±0.05
Sag DIG	0.37±0.04	0.92±0.05	0.72±0.03	0.95±0.03	0.48±0.05
UGC 8508	1.24±0.09	0.40±0.06	0.97±0.06	0.62±0.02	0.46±0.05
WLM	0.97±0.02	1.22±0.04	0.88±0.02	1.62±0.06	0.47±0.05
Haro 29	0.80±0.09	1.64±0.22	0.75±0.07	1.84±0.08	0.43±0.04
Haro 36	1.51±0.11	0.97±0.14	0.82±0.06	1.32±0.05	0.49±0.06
Mrk 178	0.68±0.09	0.68±0.07	0.71±0.05	0.79±0.02	0.55±0.05
VIIZw403	1.15±0.08	0.76±0.09	0.93±0.05	1.10±0.04	0.44±0.05

^a $R_{50,\text{HI}}$ is the radius that contains 50% of the H I of the galaxy, and $R_{90,\text{HI}}$ contains 90%. The uncertainties in these radii are determined from finding the radius at the indicated H I mass plus and minus its uncertainty. The uncertainty in the H I mass depends on the channel rms given by Hunter et al. (2012), the typical FWHM of the line profile in channels, and the area integrated.

Table 3. FUV interior and exterior to R_{Br}

Galaxy	Break Type ^a	log Interior/Exterior ^b	
		FUV/Area	FUV/V
CVnIdwA	FI	1.05 ± 0.19	0.42 ± 0.07
DDO 43	II	0.89 ± 0.03	-0.19 ± 0.05
DDO 46	II	1.02 ± 0.04	-0.11 ± 0.03
DDO 47	I
DDO 50	II	0.84 ± 0.02	-0.21 ± 0.01
DDO 52	II	0.61 ± 0.07	-0.06 ± 0.11
DDO 53	FI	1.41 ± 0.08	0.54 ± 0.01
DDO 63	FI	0.69 ± 0.01	0.13 ± 0.02
DDO 69	FI	0.77 ± 0.03	0.08 ± 0.01
DDO 70	FI	1.03 ± 0.07	0.21 ± 0.01
DDO 75	FI	0.56 ± 0.01	-0.02 ± 0.01
DDO 87	II	0.47 ± 0.11	-0.27 ± 0.02
DDO 101	II	0.74 ± 0.04	0.04 ± 0.03
DDO 126	FI+II	0.66 ± 0.05	-0.04 ± 0.01
DDO 133	II	1.11 ± 0.04	0.06 ± 0.04
DDO 154	II	0.68 ± 0.04	-0.05 ± 0.01
DDO 155	FI
DDO 165	II
DDO 167	II	1.08 ± 0.08	0.28 ± 0.04
DDO 168	FI	0.91 ± 0.01	0.16 ± 0.01
DDO 187	II	1.06 ± 0.03	0.20 ± 0.02
DDO 210	I
DDO 216	II	1.69 ± 0.92	0.69 ± 0.92
F564-V3	II	0.39 ± 0.06	-0.16 ± 0.05
IC 10	III
IC 1613	II	0.87 ± 0.02	0.01 ± 0.00
LGS 3	II	1.20 ± 0.48	0.75 ± 0.48
M81dwA	FI	0.50 ± 0.02	-0.04 ± 0.06
NGC 1569	III	1.68 ± 0.03	0.42 ± 0.02
NGC 2366	II	1.21 ± 0.01	0.15 ± 0.00
NGC 3738	III	2.15 ± 0.02	0.87 ± 0.02
NGC 4163	III	2.19 ± 0.04	0.67 ± 0.02
NGC 4214	III	1.62 ± 0.01	0.05 ± 0.00
SagDIG	II	0.92 ± 0.13	0.22 ± 0.10
UGC 8508	II
WLM	II	1.10 ± 0.03	0.32 ± 0.00
Haro 29	III	1.75 ± 0.08	0.01 ± 0.10
Haro 36	II	1.46 ± 0.03	0.86 ± 0.02
Mrk 178	FI+III	1.30 ± 0.02	0.31 ± 0.01
VIIZw 403	III	1.67 ± 0.08	0.76 ± 0.08

^aType of surface brightness profile break in the V -band (Herrmann et al. 2013). "FI" refers to a profile in which there is a short central segment that is flat or rising and then the profile drops off exponentially. "II" refers to a downward break, and "III" to an upward bend. "FI+II"

or "FI+III" refers to a profile with two breaks. "I" means that the profile does not show any break. Galaxies without breaks and those without FUV images do not have ratios of FUV interior to exterior of the break.

^bThe FUV flux is normalized by the area over which it is measured, "FUV/Area," or by the V -band flux measured over the same area, "FUV/ V ." The ratio that is given is FUV/Area or FUV/ V measured interior to the surface brightness profile break to that measured exterior to the break.

3.3. FUV Intensity Profiles

The FUV radial profiles were also fit with Sersic functions. The profile measurements and fitted curves are shown in Figure 2 in blue and the parameter results are in Table 4. The Sersic fit parameters are $\log \mu_{\text{FUV}}^0$, $R_{0,\text{FUV}}$, and n_{FUV} .

3.4. HI Rotation Curves

Oh et al. (2015) have determined the rotation curves of a subset of the LITTLE THINGS galaxies. We include 17 of those galaxies in this analysis. The remaining rotation curves were excluded for one or several of the following reasons: 1) visually, they did not have a horizontal velocity asymptote, so that although a fit was possible, at most only lower bounds for several parameters could be obtained from the data, 2) they had a profile with 3 distinct sections, which could not be fit well, or 3) they were concave with no flat section. For the galaxies included here, we fit the rotation curve with the following function, motivated by Courteau (1997):

$$V(R) = V_c \frac{(1 + \frac{R_t}{R})^\beta}{(1 + (\frac{R_t}{R})^\gamma)^{1/\gamma}} \quad (5)$$

The fit parameters are V_c , the asymptotic velocity at large radii; R_t , the transition radius at which the increase in rotation speed with radius ends; γ , which regulates the sharpness of the transition; and β , which allows for a downward slope in the outer galaxy. We fit both with β as a free parameter and with fixed $\beta = 0$. The fits were similar, so we elected to work with the $\beta = 0$ fits. We assume that $V(0) = 0$. The python function `SCIPY.OPTIMIZE.CURVE_FIT` was used to fit the data, and the uncertainties in the fitting parameters were given by the diagonal components of the covariance matrix.

The rotation curve fit parameters are given in Table 5 and their fits are shown in Figure 3. In some cases a data point or two, usually at the end, in the rotation curve were inconsistent with the rest of the points and they were eliminated from the fit. Additionally, DDO 46 and DDO 168 showed asymptotically flat behavior with a concave section at large radii. Although β allows for some concavity in the rotation curve, we were unable to fit the entire rotation curve and so fit only the portion of the rotation curve interior to the concave section. Similarly, DDO 216’s rotation curve plateaus and then begins rising again at larger radii, and the rising outer part of the curve is not included in the fit.

Table 4. Sersic Fit Parameters for FUV Profiles

Galaxy	$\log \mu_{FUV}^0$ (mag arcsec ⁻²)	$R_{0,FUV}$ (kpc)	n_{FUV}
CVnIdwA	24.96 ± 0.37	0.55 ± 0.03	0.52 ± 0.09
DDO 43	24.93 ± 0.05	2.91 ± 0.03	0.47 ± 0.01
DDO 46	24.65 ± 0.27	0.95 ± 0.05	0.71 ± 0.09
DDO 47	25.36 ± 0.14	1.72 ± 0.07	0.85 ± 0.12
DDO 50	24.01 ± 0.07	2.29 ± 0.04	0.57 ± 0.06
DDO 52	25.94 ± 0.16	2.20 ± 0.12	0.55 ± 0.14
DDO 53	23.31 ± 0.33	0.28 ± 0.01	1.06 ± 0.07
DDO 63	25.50 ± 0.14	1.61 ± 0.05	0.43 ± 0.09
DDO 69	25.88 ± 0.12	0.44 ± 0.01	0.45 ± 0.05
DDO 70	23.73 ± 0.13	0.28 ± 0.01	1.02 ± 0.06
DDO 75	24.61 ± 0.11	0.98 ± 0.02	0.21 ± 0.07
DDO 87	26.79 ± 0.15	2.72 ± 0.11	0.50 ± 0.12
DDO 101	26.70 ± 0.23	1.40 ± 0.05	0.34 ± 0.06
DDO 126	25.35 ± 0.13	1.60 ± 0.05	0.55 ± 0.08
DDO 133	25.92 ± 0.14	1.81 ± 0.03	0.41 ± 0.05
DDO 154	24.72 ± 0.07	1.13 ± 0.02	0.50 ± 0.04
DDO 167	24.08 ± 0.37	0.27 ± 0.02	0.64 ± 0.07
DDO 168	24.57 ± 0.10	1.23 ± 0.02	0.62 ± 0.04
DDO 187	24.31 ± 0.16	0.22 ± 0.01	0.79 ± 0.04
DDO 210	25.82 ± 0.24	0.17 ± 0.01	0.67 ± 0.05
DDO 216	25.30 ± 0.48	0.10 ± 0.01	1.47 ± 0.19
F564-V3	26.79 ± 0.01	1.27 ± 0.01	0.47 ± 0.01
IC 1613	24.76 ± 0.17	0.89 ± 0.02	0.60 ± 0.05
LGS 3	28.84 ± 0.25	0.22 ± 0.02	0.76 ± 0.27
M81dwA	26.16 ± 0.16	0.67 ± 0.02	0.26 ± 0.07
NGC 1569	14.22 ± 0.41	0.0019 ± 0.0002	2.94 ± 0.13
NGC 2366	23.71 ± 0.17	1.59 ± 0.05	0.81 ± 0.07
NGC 3738	15.47 ± 0.59	0.0008 ± 0.0001	3.23 ± 0.15
NGC 4163	14.42 ± 0.64	0.00 ± 0.00	4.17 ± 0.25
NGC 4214	20.41 ± 0.16	0.19 ± 0.01	1.61 ± 0.09
Sag DIG	24.42 ± 0.11	0.41 ± 0.01	0.62 ± 0.04
WLM	24.35 ± 0.15	0.61 ± 0.02	0.75 ± 0.04
Haro 29	20.43 ± 0.40	0.07 ± 0.01	1.52 ± 0.12
Haro 36	20.37 ± 0.18	0.15 ± 0.01	1.56 ± 0.06
Mrk 178	22.31 ± 0.32	0.17 ± 0.01	1.08 ± 0.09
VIIZw403	21.49 ± 0.29	0.09 ± 0.01	1.25 ± 0.08

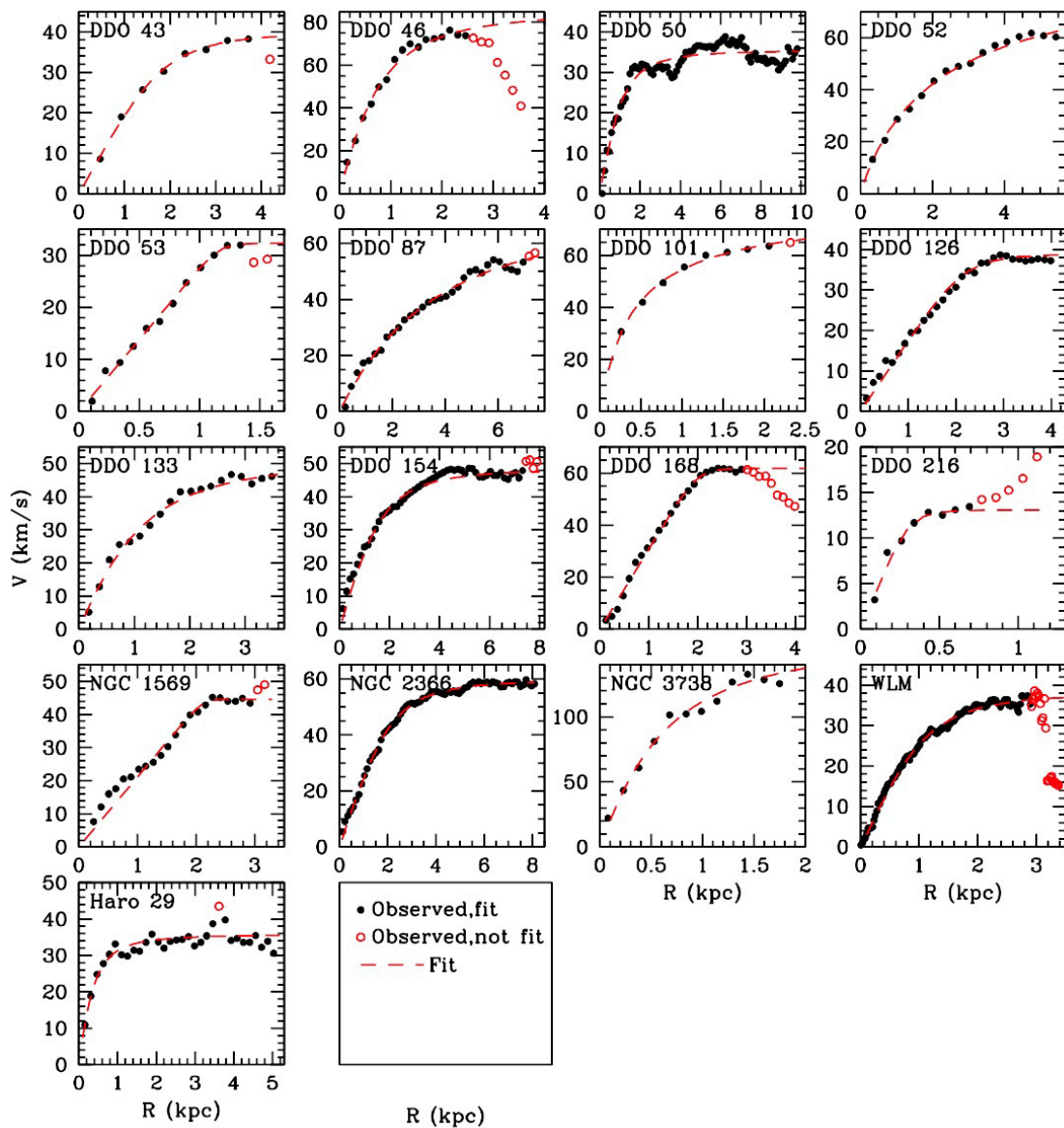


Fig. 3.— Rotation curves from Oh et al. (2015) with fits from Equation 5 with $\beta = 0$ superposed as dashed lines. Open red points were omitted from the fit.

Table 5. Rotation Curve Fit Parameters

Galaxy	R_t (kpc)	V_c (km s $^{-1}$)	γ
DDO 43	2.01±0.07	39.9±1.3	3.15±0.65
DDO 46	0.95±0.05	85.9±4.8	1.63±0.29
DDO 50	1.30±0.09	35.5±0.5	2.00±0.25
DDO 52	2.00±0.10	91.7±10.6	0.89±0.13
DDO 53	1.17±0.02	32.3±0.6	17.65±8.64
DDO 87	4.18±0.34	76.8±13.0	1.22±0.34
DDO 101	0.38±0.05	78.5±6.3	0.94±0.18
DDO 126	2.23±0.05	38.8±0.8	5.72±1.15
DDO 133	1.38±0.10	52.0±3.3	1.69±0.38
DDO 154	1.93±0.10	48.3±0.6	2.30±0.27
DDO 168	2.02±0.02	61.9±0.5	10.97±1.84
DDO 216	0.32±0.04	13.1±1.3	5.07±4.81
NGC 1569	2.11±0.05	44.6±0.5	20.88±15.38
NGC 2366	2.38±0.03	59.5±0.3	2.69±0.12
NGC 3738	0.76±0.17	160.9±37.3	1.43±0.91
WLM	1.27±0.03	38.0±0.5	2.55±0.23
Haro 29	0.47±0.06	35.8±0.9	1.76±0.39

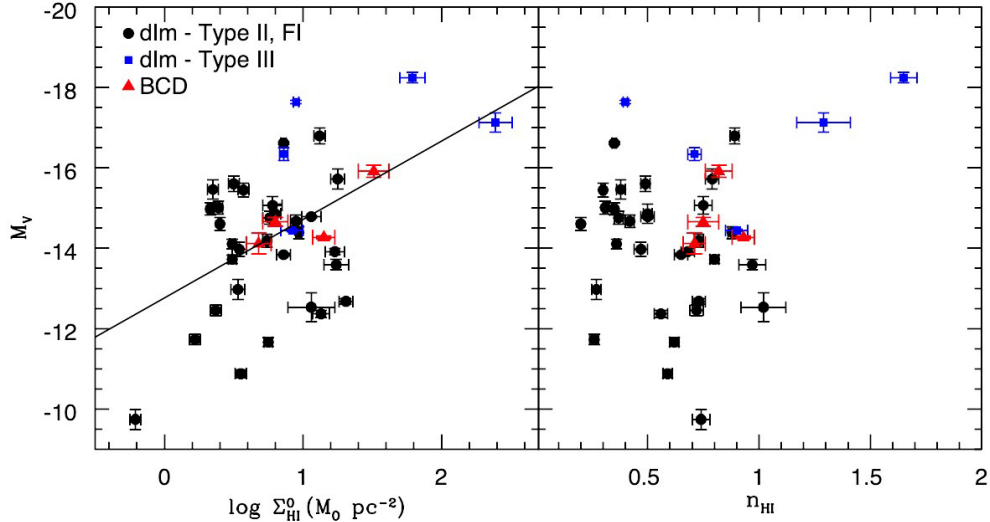


Fig. 4.— Integrated galactic M_V plotted against Sersic parameters $\log \Sigma_{\text{HI}}^0$ and n_{HI} that describe the HI surface density profile. There is a trend $M_V = (-12.77 \pm 0.52) - (1.95 \pm 0.55) \log \Sigma_{\text{HI}}^0$, correlation coefficient 0.5, standard deviation 1.5. The trend is in the sense that more luminous dwarfs have higher central atomic gas densities. There is no trend of M_V with n_{HI} correlation coefficient of 0.2).

3.5. Summary of parameters

In Section 3 we have described the parameters that we use to characterize the stellar, gas, and star formation surface density profiles and related parameters for purposes of examining the relationships between these galactic components. The parameters are listed and described as a reference to the reader in Table 6.

4. Results

4.1. Comparisons with HI surface density profiles

4.1.1. M_V

In Figure 4 we plot integrated galactic M_V against key Sersic parameters: $\log \Sigma_{\text{HI}}^0$ and n_{HI} . We see that there is a trend of M_V with $\log \Sigma_{\text{HI}}^0$, with a correlation coefficient of 0.5. The relationship ($M_V = (-12.77 \pm 0.52) - (1.95 \pm 0.55) \log \Sigma_{\text{HI}}^0$) is one in which more luminous dwarfs tend to have higher central atomic gas densities. There is no trend of M_V with n_{HI} , the parameter that describes how the gas falls off with radius.

Table 6. Summary of disk parameters

Disk component	Quantity	Description	Note	Ref
HI	$\log \Sigma_{\text{HI}}^0$	Extrapolated central surface mass density	Sersic fit	Table 2
	$R_{0,HI}$	Characteristic radius	Sersic fit	Table 2
	n_{HI}	Curvature of profile	Sersic fit	Table 2
	$(R_{50}/R_{90})_{HI}$	Central concentration of HI	Low ratio for more central concentration	Table 2
Stars	R_D	Disk scale length		Herrmann et al. (2013)
	R_{Br}	Break radius	Where the surface brightness profile changes slope	Herrmann et al. (2013)
	C_{31}	Central concentration of stellar mass	Larger C_{31} , more centrally concentrated	Zhang et al. (2012)
FUV	$\log \mu_{FUV}^0$	Extrapolated central surface brightness	Sersic fit	Table 4
	$R_{0,FUV}$	Characteristic radius	Sersic fit	Table 4
	n_{FUV}	Curvature of profile	Sersic fit	Table 4
	FUV/V before/after	Change in SF activity at R_{Br}	Ratio of normalized FUV before and after R_{Br}	Table 3
	R_{FUV}^{knot}	Radial extent of furthest FUV knot		Hunter et al. (2016)
	$\log FUV_{1R_D}/FUV_{1-3R_D}$	Concentration of SF activity	Ratio of FUV in $1R_D$ to that in $1-3R_D$	Table 1
	$\log SFR_{FUV}^{\text{int}}$	Integrated SFR	Measured in FUV, normalized to $1R_D$ area	Hunter et al. (2012)
	$R_{H\alpha}$	Radial extent of H α		Hunter & Elmegreen (2004)
	V_c	Asymptotic velocity		Table 5
	R_t	Transition radius	Where rotation speed levels off or increases slowly	Table 5
γ	Sharpness of transition		Table 5	

4.1.2. Characteristic radii

What do the parameters n_{HI} and $R_{0,HI}$ actually mean in a dwarf galaxy? In Figure 5 we plot various ratios of characteristic radii against n_{HI} . The radii we use include $R_{0,HI}$, the characteristic radius in the H I Sersic profile; $R_{H\alpha}$, the furthest radius at which H α emission is detected; R_D , the stellar disk scale length measured in V ; $R_{50,HI}$, the radius that contains half of the H I gas; and $R_{90,HI}$, the radius that contains 90% of the H I gas (see Table 2). A low ratio of $(R_{50}/R_{90})_{HI}$ indicates that the inner 50% of the H I is more centrally concentrated or that the outer 40% of the H I is more extended. There is a strong relationship between all ratios and n_{HI} . We see that galaxies with higher n_{HI} have, relative to $R_{0,HI}$, more far-flung H II regions, bigger V -band disk scale lengths, and larger $R_{50,HI}$.

The dashed lines in the bottom panels are from integrals over the Sersic function itself, $\int_0^R \exp(-[R/R_0]^{1/n}) 2\pi R dR$, and show the expected ratios of radii for H I if the H I profiles are perfect Sersic fits throughout. We see that the galaxy data generally follow the dashed curves for R_0/R_{50} vs. n_{HI} and $(R_{50}/R_{90})_{HI}$ vs. n_{HI} , including at higher n_{HI} where the dashed curve deviates from the linear fit to the galaxy points. This implies that the H I surface density profiles are well fit by a Sersic disk. The exception is in the panel for R_0/R_{50} vs. n_{HI} , at low end of n_{HI} , where the curve turns over and two galaxies (DDO 167 and IC 1613) do not follow that turnover. Both galaxies have depressions or holes in their H I in their centers. However, the gas beyond the holes is fit with a Sersic profile with very low n_{HI} , which Figure 1 shows corresponds to overall more centrally concentrated H I (at least outside the holes), and the smaller $R_{50,HI}$ relative to $R_{0,HI}$, is consistent with the gas being more centrally concentrated compared to a pure Sersic disk.

The top two panels mix optical and H I radii, and because the furthest H α region is typically at a distance of between 2 and 3 V -band disk scale lengths, the top left panel is showing about the same correlation as the top right panel. This correlation indicates that the H I scale length increases relative to the optical scale length as the H I profile becomes relatively flatter in the inner regions. In Section 4.2, we explain this correlation as the result of a conversion of H I into molecules in the inner regions, which flattens the H I profile more than the total gas profile, lowering n_{HI} and increasing $R_{0,HI}$ at the same time relative to R_D .

4.1.3. FUV radial profiles

The Sersic indices for FUV, n_{FUV} , and for HI, n_{HI} , and the scale lengths for FUV, $R_{0,FUV}$, and for HI, $R_{0,HI}$, relative to the V -band scale length, R_D , are plotted in Figure 6.

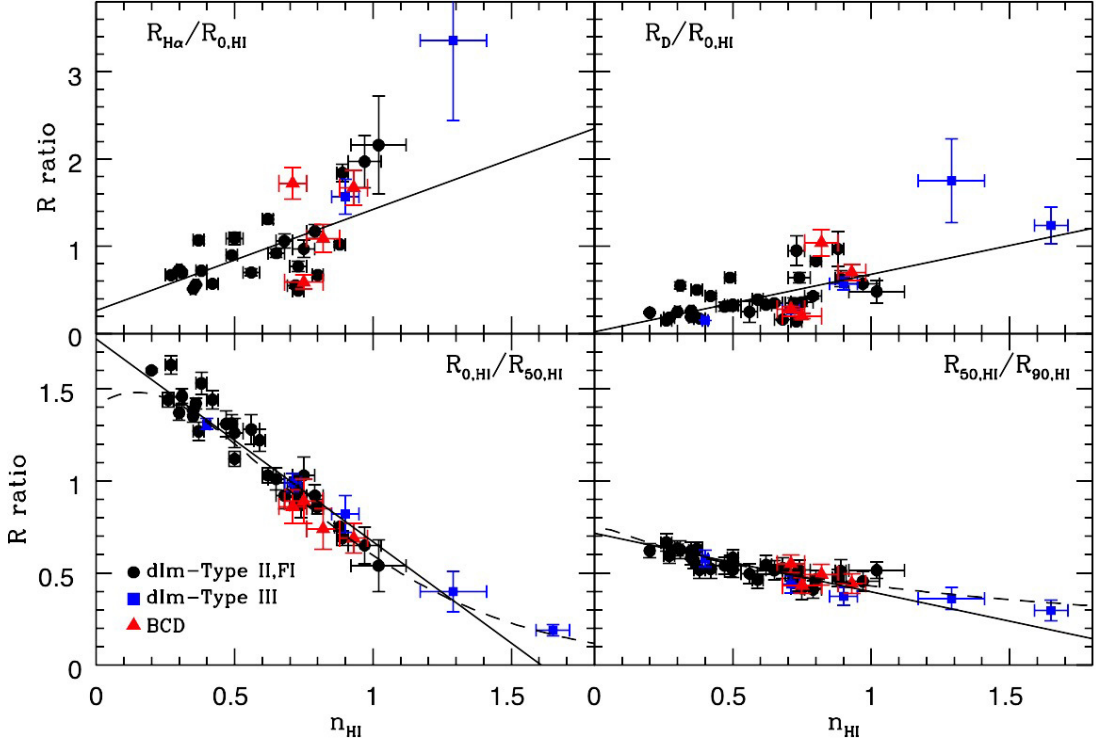


Fig. 5.— Plots of ratios of characteristic radii (see Table 2) against Sérsic n_{HI} . $R_{0,HI}$ is the normalizing radius in the HI Sérsic profile. The two most discrepant galaxies (DDO 155 and NGC 3738) are not included in the fits shown in the upper two panels. *Upper left*: $R_{H\alpha}$ is the radius at which the H II region furthest from the center of the galaxy is located. The solid line is a fit to the data: $R_{H\alpha}/R_{0,HI} = (0.26 \pm 0.20) + (1.16 \pm 0.30)n_{HI}$, and the correlation coefficient is 0.6 and the standard deviation is 0.4. Galaxies with more distant H II regions relative to $R_{0,HI}$ have higher n_{HI} . *Upper right*: R_D is the stellar disk scale length measured in V (Herrmann et al. 2013). The solid line is a fit to the data: $R_D/R_{0,HI} = (0.022 \pm 0.082) + (0.66 \pm 0.12)n_{HI}$, and the correlation coefficient is 0.7 and the standard deviation is 0.2. Bigger disk scale lengths relative to $R_{0,HI}$ are associated with higher n_{HI} HI profiles. *Lower left*: $R_{50,HI}$ is the radius that contains half of the HI gas. The solid line is a fit to the data (correlation coefficient of 0.97, standard deviation of 0.09): $R_{0,HI}/R_{50,HI} = (1.77 \pm 0.03) - (1.10 \pm 0.05)n_{HI}$. The smaller $R_{0,HI}$ is relative to $R_{50,HI}$, the bigger n_{HI} is. *Lower right*: $R_{90,HI}$ is the radius that contains 90% of the HI gas. The solid line is a fit to the data (correlation coefficient of 0.9, standard deviation of 0.04): $R_{50,HI}/R_{90,HI} = (2.26 \pm 0.15) - (3.15 \pm 0.30)n_{HI}$. The dashed curves in the lower panels are expected for a pure Sérsic disk.

Both the Sérsic indices and the scale lengths correlate with each other for the FUV and HI, with n_{HI} about 0.6 times n_{FUV} . The actual fits are $n_{HI} = (0.41 \pm 0.10) + (0.23 \pm 0.08)n_{FUV}$

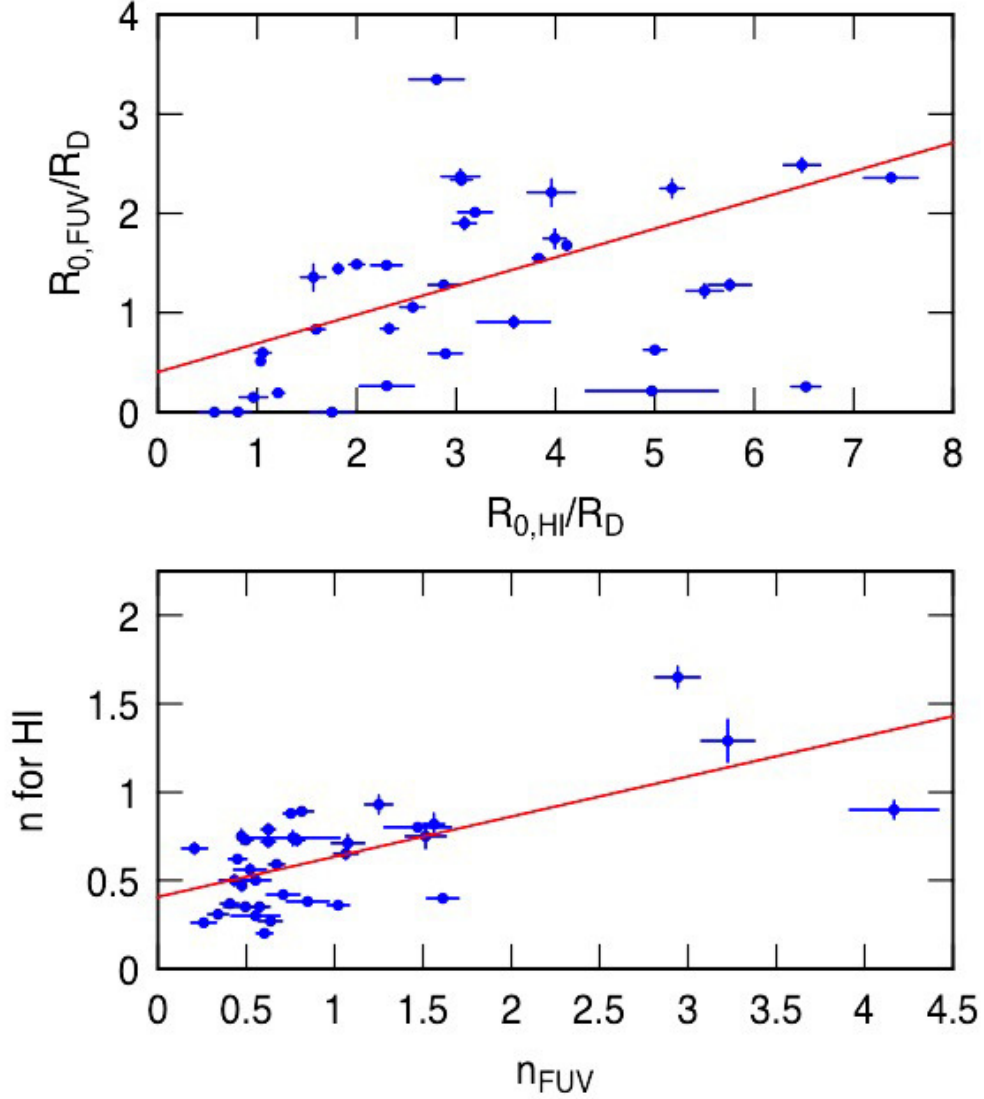


Fig. 6.— Bottom: The Sersic index for HI versus the Sersic index for FUV, showing a correlation with $n_{HI} \sim 0.6n_{FUV}$. Top: Scale length comparison for FUV ($R_{0,FUV}$) and HI ($R_{0,HI}$), relative to the V -band scale length, R_D . FUV disks average a factor of ~ 2 smaller than HI disks.

and $R_{0,FUV}/R_D = (0.40 \pm 0.71) + (0.29 \pm 0.19)(R_0/R_D)$. The correlations imply that when the HI turns over in the inner region of a galaxy (low n_{HI}), the FUV does also, although the FUV scale length is about half the HI scale length.

4.1.4. Integrated star formation rates

In the top panel of Figure 7 we show a correlation between the logarithm of the total galactic FUV SFR normalized to the area inside the V -band scale length, $\log \text{SFR}_D^{\text{FUV}}$, and the logarithm of the extrapolated central H I surface density, $\log \Sigma_{\text{HI}}^0$, from the Sersic fit. The SFR is normalized in order to compare galaxies of different sizes and masses. We see that galaxies with higher extrapolated central H I surface densities have higher galactic SFRs per unit disk area. A least-squares fit to the data yields the relationship

$$\log \text{SFR}_D^{\text{FUV}} = (-2.78 \pm 0.18) + (0.82 \pm 0.19) \log \Sigma_{\text{HI}}^0. \quad (6)$$

The rms of the fit is 0.54. Thus, the galaxy-wide area-normalized SFR is proportional to the extrapolated central H I density to the 0.8 power.

Gas in dwarf galaxies appears to be dominated by the atomic phase (Kenney & Young 1988). There should be molecules present, as observed in the SMC (Bolatto et al. 2011) and in other dwarfs such as NGC 1569 (Taylor et al. 1999) and IC 10 (Ohta et al. 1988, 1992; Wilson & Reid 1991; Leroy et al. 2006), but the molecular abundances traced by CO could be low compared to H I (e.g., Bigiel et al. 2008; Rubio et al. 2015). Most dwarfs in our survey also have a total H I mass that is larger than the stellar mass (Zhang et al. 2012), which is rarely true for spirals. Thus, the near-linear relationship between integrated SFR per unit area and extrapolated central H I density $\log \Sigma_{\text{HI}}^0$ suggests a close connection between star formation and atomic gas that is not expected for spirals. In Section 4.2, we estimate the H_2 surface density that is present in the central regions.

Figure 7 has considerable scatter in the distribution of points, so we wondered if there could be a physical origin for this scatter: are the high or low points systematically high or low because of some dependence on an additional parameter? The most obvious additional parameter is metallicity. The oxygen abundance given by $12 + \log (\text{O}/\text{H})$ varies by 1.8 dex in our sample. To examine this, we plot in Figure 7 the oxygen abundance versus the quantity $\log \text{SFR}_D^{\text{FUV}} - (-2.78 + 0.82 \log \Sigma_{\text{HI}}^0)$, which is the difference between the SFR and the average dependence on $\log \Sigma_{\text{HI}}^0$. We see no trend. This lack of a trend makes sense if most of the molecular regions are H_2 with relatively little CO, and if the H_2 always has sufficient time to form even at a low relative dust abundance. Then the relative molecular fraction would not depend much on metallicity, and the residual gas, viewed here in H I, would be relatively independent of metallicity too.

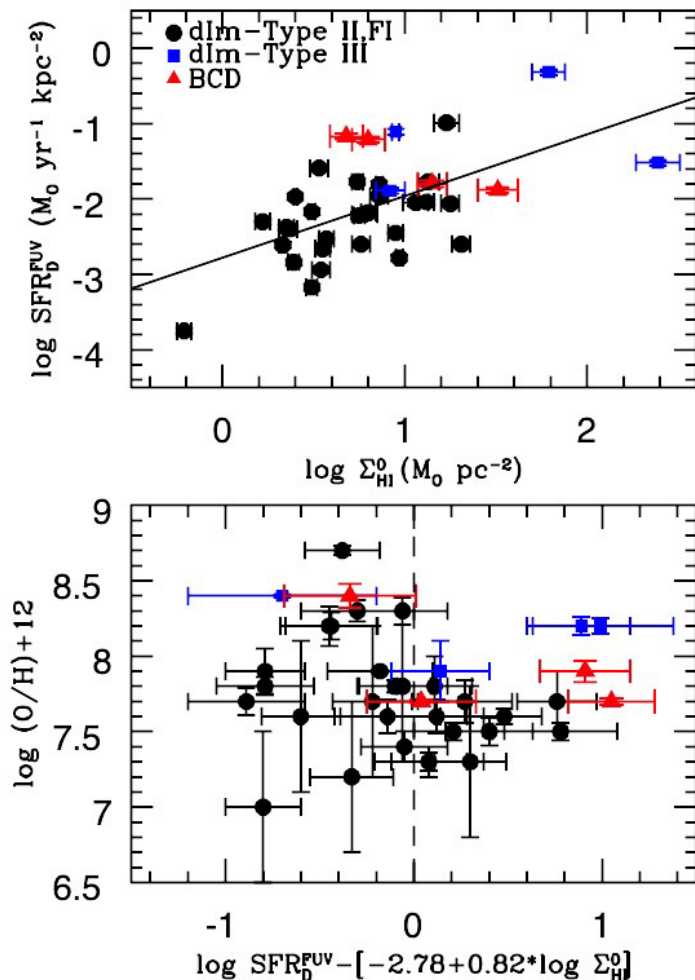


Fig. 7.— *Top*: Logarithm of the integrated SFR per unit V -band disk area plotted against the extrapolated central HI density from the Sersic fit. Uncertainties are generally smaller than the point size. The solid line is a fit to the data, with a correlation coefficient of 0.59 and standard deviation of 0.5: $\log \text{SFR}_{\text{D}}^{\text{FUV}} = (-2.78 \pm 0.18) + (0.82 \pm 0.19) \log \Sigma_{\text{HI}}^0$. If the three outliers are not include the slope becomes 0.3 ± 0.4 and the correlation coefficient is 0.12. *Bottom*: Oxygen abundance plotted against SFR minus the fit in the upper panel. The vertical dashed line delineates the locus with no scatter from the upper panel fit. There appears to be no relationship between the scatter around the fit in the upper panel and metallicity.

4.1.5. Concentration of stars and gas

An obvious connection between stars and gas would be that the more centrally concentrated the gas is, the more centrally concentrated we would expect the stars and star formation to be. With that in mind, we plot measures of the concentration of stars and star formation against n_{HI} in Figure 8. C_{31} , a measure of the central concentration of the stars, is taken from Zhang et al. (2012). It is defined as the ratio of the radii that encompass 75% and 25% of the total stellar mass (de Vaucouleurs 1977). The larger C_{31} is, the more centrally concentrated the stellar mass. Here we see a slight correlation between the central concentration of stars and the central concentration of gas as described by n_{HI} . The dashed line shows what to expect if the surface densities of stars and gas have the same Sersic profiles, i.e., evaluating C_{31} and n for a single Sersic function. The approximate agreement with the observations suggests that the central concentration of stellar mass is related to the central concentration of H I gas.

To examine the concentration of star formation, we use the ratio of the FUV flux in the central scale length to the FUV flux in an annulus around the center between 1 and 3 R_D . We denote this ratio by FUV_{1R_D}/FUV_{3-1R_D} in the bottom panel of Figure 8. The higher the ratio, the more centrally concentrated is the star formation activity. The figure indicates that higher SFR concentration corresponds to higher n_{HI} .

However, this bottom panel contains a mixture of galaxy properties; it determines the FUV amounts inside various V -band scale lengths as a function of the shape of the H I profile. We examine this issue further in Figure 9. The decreasing curve in this figure shows the ratio of the flux inside one scale length to that between 1 and 3 scale lengths versus the Sersic index for a pure Sersic profile. The points in Figure 9 are a result of integrating Sersic fits to the FUV for each galaxy to the V -band radius R_D and between 1 and 3 R_D and plotting the ratio of these versus both the H I Sersic index n_{HI} (blue x marks) and the FUV Sersic index, n_{FUV} (red dots). The blue x marks are similar to the points plotted in Figure 8 determined observationally, and the distribution of points from the integrals agrees with the distribution of values from the observations in Figure 8. However, the red dots are more self-consistent, because they are the integral of the FUV versus the FUV fit parameter n_{FUV} . The blue crosses, which are versus n_{HI} , agree pretty well with the pure FUV red dots because the H I n_{HI} and the FUV n_{FUV} scale with each other, as shown in Figure 6. From this we conclude, that the correlation we see in the bottom panel of Figure 8 is reasonable even though the quantities mix the FUV, V , and H I galaxy properties.

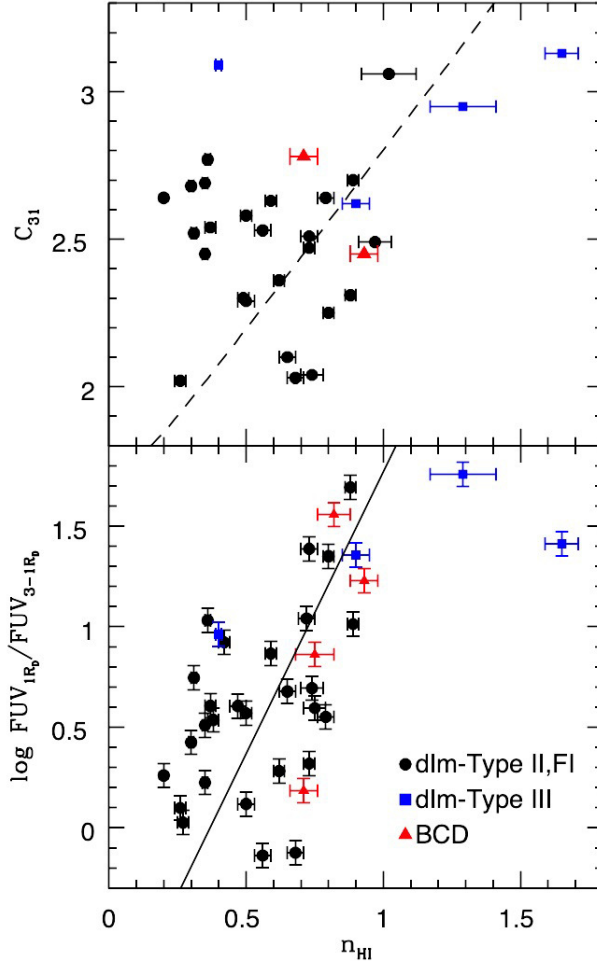


Fig. 8.— *Top*: Plot of stellar concentration index C_{31} (Zhang et al. 2012) against n_{HI} . Higher C_{31} means a higher central concentration of stars. The dashed line shows what to expect if the surface densities of stars and gas have the same Sersic profiles and is not a fit to the data. *Bottom*: Ratio of FUV emission within one disk scale length R_D to that within the annulus bounded by $1-3R_D$ plotted against n_{HI} . The higher the ratio FUV_{1R_D}/FUV_{3-1R_D} , the more centrally concentrated the FUV emission, and hence star formation. Here we see a correlation in the sense that the more centrally concentrated the star formation, the higher is n_{HI} . The solid line (correlation coefficient 0.61 and standard deviation of 0.4) is $n_{HI} = (0.37 \pm 0.07) + (0.36 \pm 0.08) \log FUV_{1R_D}/FUV_{3-1R_D}$.

4.2. Flat H I surface density profiles and “dark” gas

The family of Sersic profiles that fit the H I surface density in LITTLE THINGS dIrr galaxies are generally flatter than exponential because $n_{HI} = 0.2$ to 1 for the H I and a pure exponential would have $n_{HI} = 1$ (see Figure 1). The H I profiles are also flatter than the FUV surface brightness profiles (see Figure 6). Could the flatness of the H I profile be an indication of the presence of “dark” gas, gas that is molecular, and hence not detected in H I, but not detected in CO observations yet either? We suggested there was a significant

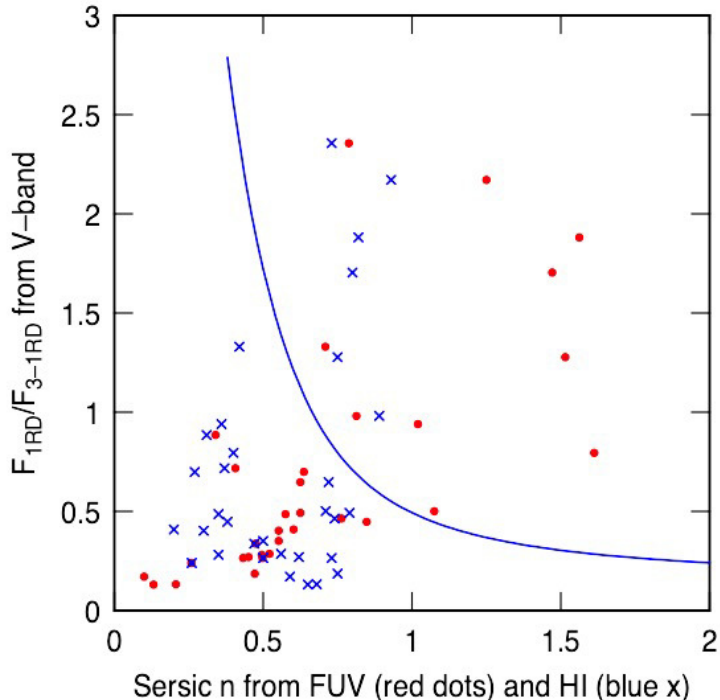


Fig. 9.— An examination of the origin of the correlation in the bottom panel of Fig 8. The curve shows the ratio of the flux inside one scale length to that between 1 and 3 scale lengths versus the Sérsic index for a pure Sérsic profile. This curve does not agree with the observations in the previous figure which mix together all three profiles: FUV, V , HI. The points use the fitted Sérsic profiles for FUV for each galaxy, with the ratio of the integral of the FUV flux inside the V -band scale length to that between 1 and 3 scale lengths plotted versus the HI Sérsic index (blue x marks) and the FUV Sérsic index (red dots).

fraction of H_2 , 23% of the gas on average, in our sample of dIrr galaxies on the basis of strong FUV emission and star formation activity away from the regions where there are prominent HI clouds (Hunter et al. 2019a).

We examine this possibility again here in two ways. First, we return to the top-right panel of Figure 5 which shows the ratio of the V -band scale length R_D to the HI scale length $R_{0,HI}$ versus the HI Sérsic index n_{HI} . These data points are reproduced in Figure 10 where we superimpose model curves that attempt to fit the range of points. The models have molecular fractions at the galaxy center that range from 5% to 100%. For the 5% fractions, the model HI profile is essentially the total gas profile, and these models correspond to the upper right-hand positions of each curve. The curves then trace down and to the left as the central molecular fraction increases. Thus when the Sérsic index for HI is 1 on the abscissa, like the V -band profile which has an index close to 1, the two profiles, total gas and V -band, have about the same shape. The different curves that reach $n_{HI} = 1$, which are the red

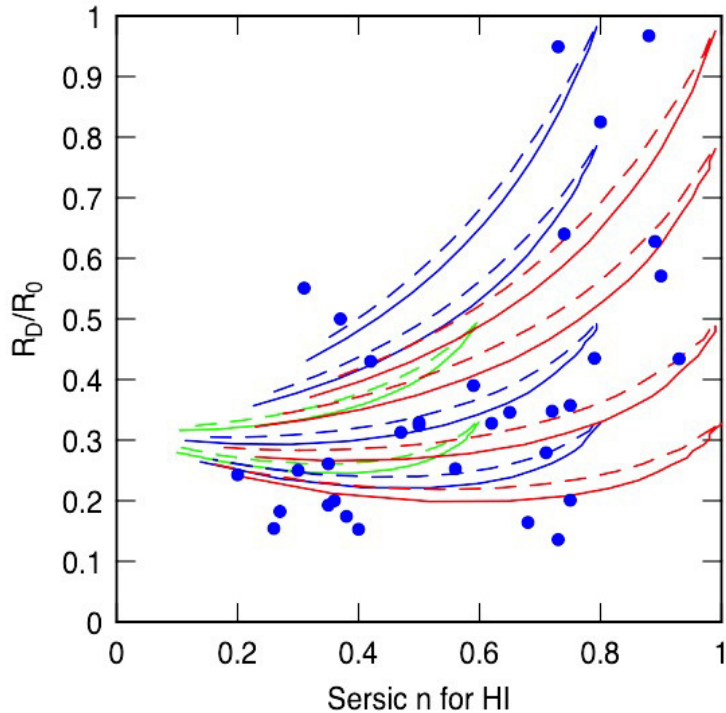


Fig. 10.— Comparison of observations of $R_D/R_{0,HI}$ from the upper right panel of Figure 5, plotted as points, with models for total gas Sersic disks that become molecular in the inner regions. The difference between the total and the molecular gas represents H I, and this H I is fitted to a Sersic profile with the parameters plotted here. The molecular fraction of total gas varies from 5% at the upper right end of each curve to 100% at the lower left. The molecular surface density is assumed to be proportional to the total gas surface density to the power 1.5 (solid curves) or 2 (dashed curves), in accord with dynamical models of molecular cloud formation. The different colored curves show different intrinsic n_{HI} for the total gas (right-hand limit; red 1, blue 0.8, and green 0.6) and different intrinsic ratios of R_D to $R_{0,HI}$ (upper limits), increasing as one goes up the figure. The models span the range of parameters given by the observations. This suggests that the Sersic index n_{HI} for H I is lower than for the optical disk and the scale length for H I is higher than for the optical disk because of systematic conversions of H I to molecules in the inner regions of these galaxies.

curves, show different intrinsic ratios of V -band to H I scale lengths, ranging from 0.33 to 1 as one goes up the figure. Similarly, the other curves have right-hand limits at the intrinsic H I Sersic index in the model and they have upper limits at the intrinsic ratio $R_D/R_{0,HI}$.

To trace out the rest of the curves we assume that the H_2 surface density is proportional to the total gas surface density to the 1.5 power (solid curves) or 2.0 power (dashed curves), from the Kennicutt-Schmidt relation that follows from a dynamical model for molecular cloud formation (Elmegreen 2015b, 2018). In this model, the rate of conversion of total gas

into dense gas, traced by CO or H₂, is the dynamical rate at the midplane density of total gas. For the 1.5 power, the disk thickness varies more slowly with radius than the surface density, as in several ULIRGS studied by Wilson et al. (2019) and the main parts of spiral galaxies (Elmegreen & Elmegreen 2020). For the 2.0 power, the gas disk flares with radius because it is self-gravitating with a nearly constant velocity dispersion (Elmegreen 2018). The H I surface density is then taken to be the total gas minus the H₂. Sersic fits to this H I surface density are given by the curves. As the H₂ fraction increases, the H I profile flattens, lowering n_{HI} , and the H I scale length increases, lowering the ratio $R_D/R_{0,HI}$. The observations are traced out well by this model.

A second way to test for the presence of molecules is to use the Sersic fit to the FUV intensity for each galaxy and convert it to a radial profile of SFR density, Σ_{SFR} , and then convert this SFR density profile to a molecular density profile by multiplying it by a constant molecular gas consumption time of 2×10^9 years (Leroy et al. 2008). According to the dynamical model of star formation (Elmegreen 2018), the molecular consumption time is different from the dynamical time at the midplane, used above for the relation between Σ_{SFR} and total gas, because the consumption time is related to the dynamical time at the characteristic density of the molecular material (multiplied by the inverse of some efficiency), which is much higher than the average midplane density except in starburst galaxies. Whether the molecular material is observed in CO, as for spirals, or not observed in CO, as for dIrrs, presumably depends on the metallicity, which is much lower in dIrrs (Rubio et al. 2015).

The projected SFR density is derived from the projected FUV intensity using the relation:

$$\Sigma_{SFR} = 10^{-0.4\mu_{FUV}+7.155} M_{\odot} \text{ pc}^{-2} \text{ Myr}^{-1}, \quad (7)$$

which assumes negligible dust extinction, a Chabrier stellar initial mass function (Chabrier 2003), and the calibration in Kennicutt (1998), modified for sub-solar metallicities by Hunter et al. (2010). The FUV surface brightness in magnitudes per square arcsec is denoted by μ_{FUV} and comes from the Sersic fit to the FUV.

The projected molecular density profile obtained from the FUV intensity in this way is then added to the observed projected H I Sersic profile to get the total gas total projected gas profile. All three gas profiles are shown in Figure 11. Figure 12 shows the radial profiles of the molecular fraction, obtained from the ratio of the projected molecular surface density to the total. The molecular fractions are typically high in the center where the star formation rate is higher than expected if all of the gas is from the observed H I surface density. The average molecular fraction for all galaxies, measured out to $3R_D$, is 0.23 ± 0.17 , as obtained from the ratio of $\int \Sigma_{H_2} 2\pi R dR$ to $\int \Sigma_{\text{sum}} 2\pi R dR$.

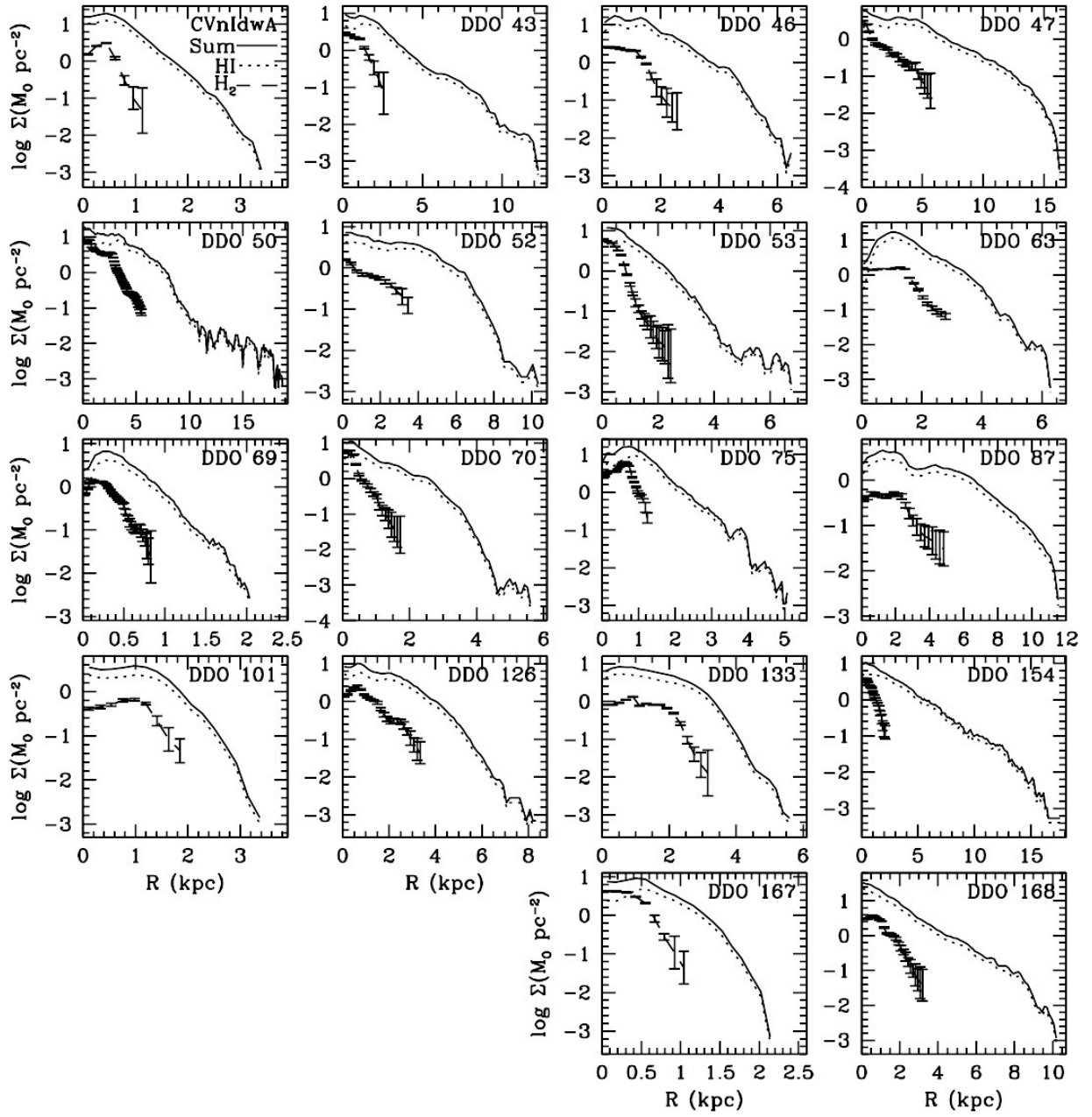
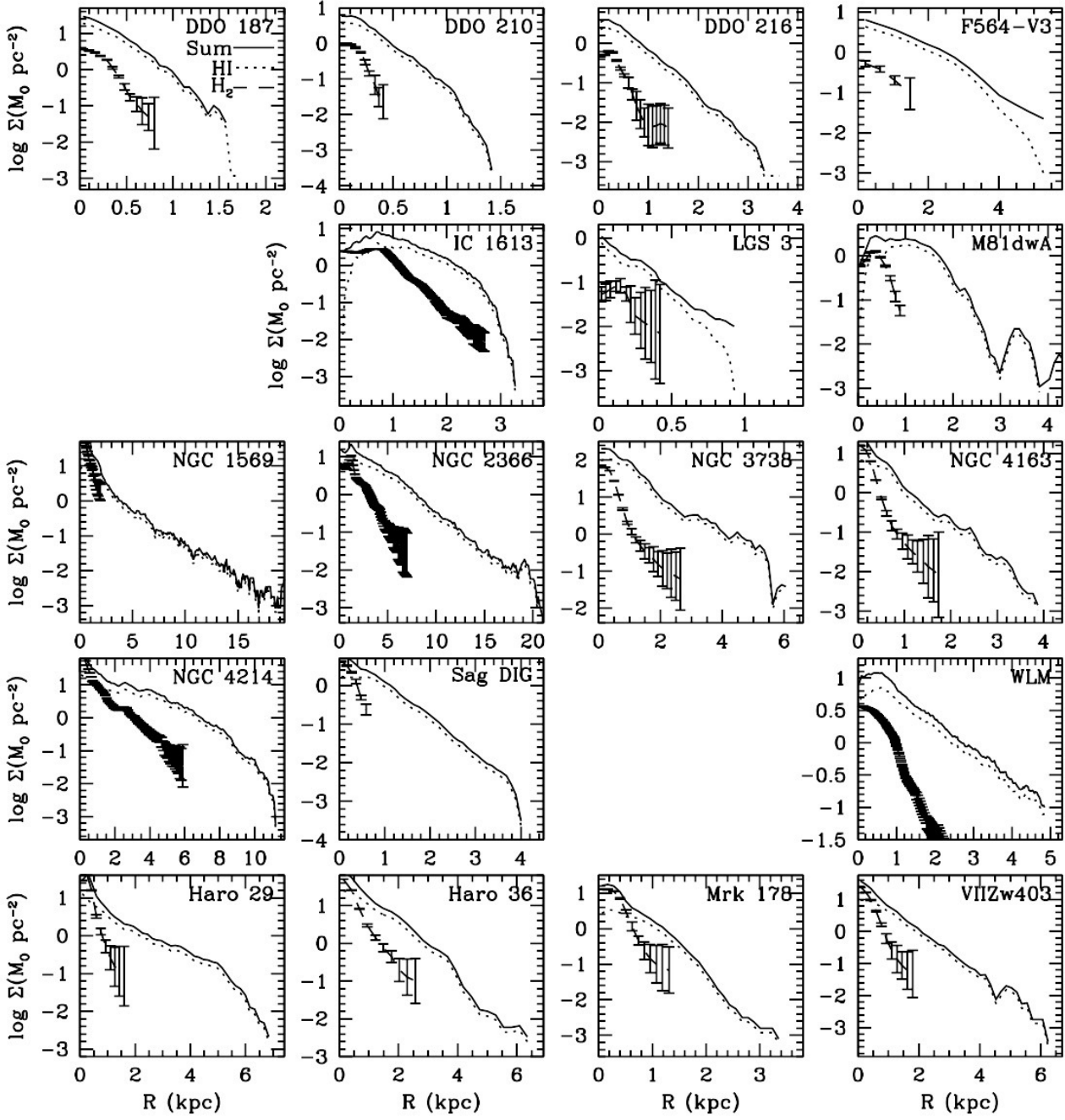


Fig. 11.— Logarithm of the sum H I+He+H₂ surface density profiles (solid lines), the H I surface density (dotted lines), and the H₂ surface density profiles inferred from the FUV (dashed lines). Helium is taken to be 34% of H I, and the H₂ is inferred from the FUV emission as discussed in the text. The uncertainties in the H₂ profiles are the uncertainties of the logarithm of the FUV flux. The blanks in the plots are the galaxies without FUV data (DDO 155, DDO 165, IC 10, UGC 8508) and are maintained to facilitate comparison with Figure 2.



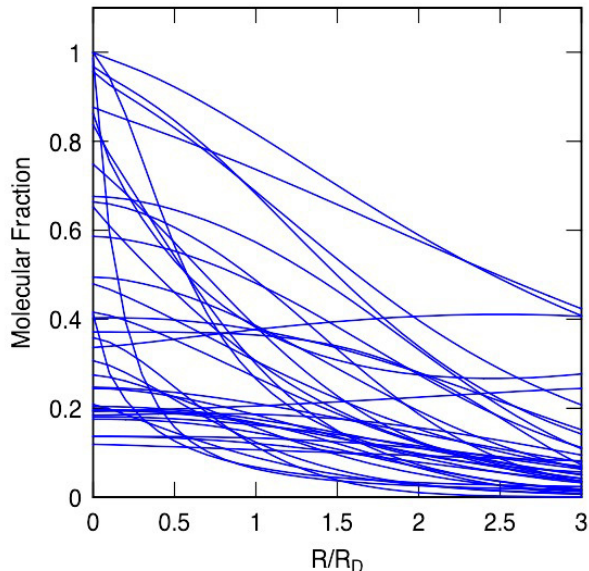


Fig. 12.— Radial profiles of model molecular fractions obtained by converting the FUV surface brightness to molecular surface density and dividing by the sum of this surface density and the H I surface density.

5. Investigating R_{Br}

A ubiquitous but perplexing feature of stellar radial profiles is a sharp change in the slope of the exponential fall-off. This is a feature of most exponential disks, both spiral and dwarf irregular. Here we explore connections between R_{Br} and other radial attributes of the dIrr galaxies.

5.1. Comparison with H I profiles

In Figure 13 we plot the radius at which the V -band surface brightness profile changes slope R_{Br} against the Sersic parameter n_{HI} . The R_{Br} are normalized by R_0 from the Sersic fit to the H I surface density profile. For most galaxies, R_{Br} is smaller than $R_{0,HI}$. However, there is a modest increase in R_{Br} relative to $R_{0,HI}$ around $n_{HI} = 1$. The three galaxies with high values of $R_{Br}/R_{0,HI}$ also have high uncertainties in this quantity. The origin of the relationship in Figure 13 is probably similar to that in the top-left of Figure 5, namely, R_{Br} increases with the size of the galaxy. (See also Section 5.5 below where we show that the ratio of R_{Br} to R_D is approximately a constant: $R_{Br}/R_D \sim 0.5-2$).

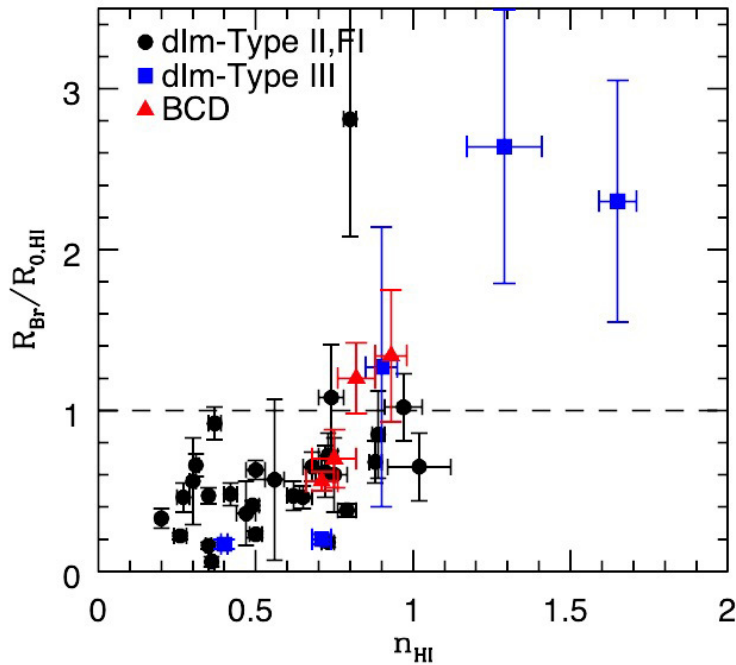


Fig. 13.— Break radius R_{Br} from the V -band surface brightness profile normalized by $R_{0,\text{HI}}$ plotted against n_{HI} . The correlation coefficient is 0.7 and the standard deviation is 0.5. The dashed horizontal line marks the ratio corresponding to $R_{\text{Br}}=R_{0,\text{HI}}$.

5.2. Comparisons with HI rotation curves

In Figure 14 we plot parameters that characterize the fit to the HI rotation curve against the break radius R_{Br} in kiloparsecs. A strong correlation between R_{Br} and the transition radius R_t or the sharpness of the transition γ would point to an underlying kinematic explanation of the breaks in dwarf galaxy surface brightness profiles. The solid line in the top panel denotes $R_t = R_{\text{Br}}$. There we see a lot of scatter around the line of equality. The other two panels do not show correlations.

A different correlation in Figure 14 indicates that larger galaxies, with larger rotation speeds and larger R_{Br} , have smoother-rising rotation curves. This is also evident directly from Figure 3. Generally we consider larger galaxies to be earlier Hubble types with bulges and more rapidly rising inner rotation curves, which would give them lower γ . This is not the case in the dIrr class. Possibly we are seeing that strong feedback from early central star formation scatters the central mass and broadens its concentration more for more massive dIrrs (Governato et al. 2012; El-Badry et al. 2016), as that would make the inner rotation curve rise more slowly.

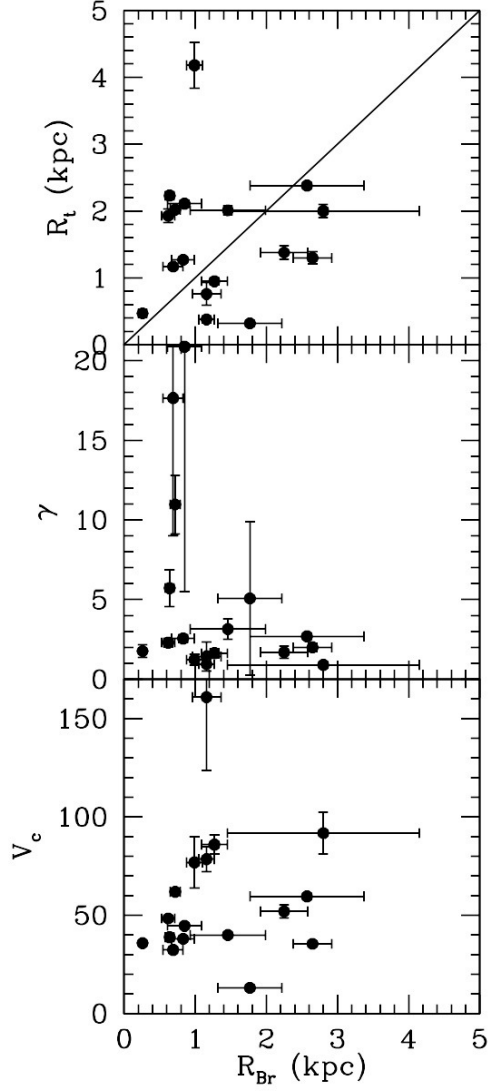


Fig. 14.— Parameters from the fit to the HI rotation curve plotted against the break radius R_{Br} . The solid line in the top panel denotes $R_t = R_{Br}$ and is not a fit to the data. The correlation coefficient of the data in the top panel is 0.04 and the standard deviation is 0.95.

5.3. Star formation activity interior and exterior to R_{Br}

In Figure 15 we show histograms of the ratio of FUV emission interior to R_{Br} to that exterior to R_{Br} . The values for the spiral galaxies that were included in this study are marked by spiral morphological type. Two normalizations of the FUV flux are shown: to the area over which the flux is integrated and to the V -band flux integrated over the same area as for the FUV. We separate galaxies whose profiles bend downward (Type II and FI) from those that bend upward (Type III).

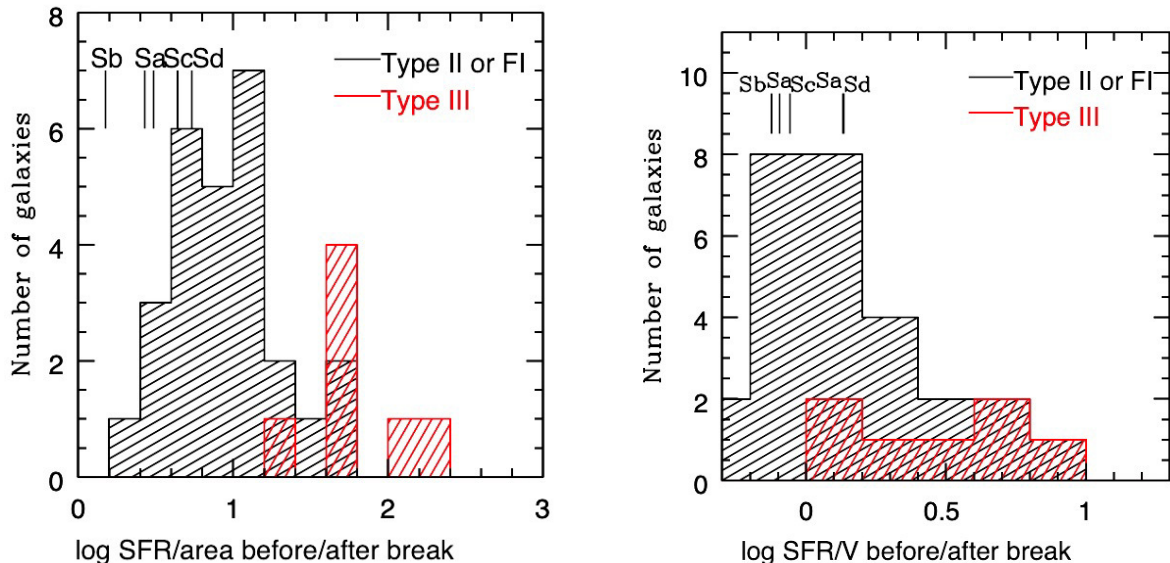


Fig. 15.— Number of galaxies with given ratios of FUV flux integrated interior to R_{Br} to that exterior to R_{Br} . Two normalizations are used: area included in the integration (left) and V -band flux in the same region integrated (right). Values for our spiral galaxy sample are indicated by morphological type of the galaxy, and Type II or FI dIrr are plotted separately from Type III.

For the dIrrs the ratios with the V -band normalization vary from 0.53 (DDO 87) to 7.5 (NGC 3738) with a median value of 1.4. However, down-bending types tend to have lower ratios than up-bending types. The number of spirals is small and thinly divided by morphological type, but all five have down-bending profiles and have ratios that are typical of the down-bending dwarfs. Thus, the down-bending dIrr and spirals have approximately the same amount of normalized star formation interior to R_{Br} as exterior, while the up-bending dIrr have more centrally concentrated star formation. For the area normalization, up-bending types also have higher ratios than down-bending types, but the spirals tend towards lower values than typical of the dIrrs. Thus, we see that the star formation activity, relative to the integrated light of older stars, in many dIrr galaxies with a down-bending profile does not change drastically at the break, while those with up-bending profiles have systematically more star formation interior to the break. Interestingly, the spirals are similar to those of the majority of the down-bending dIrr galaxies, suggesting that in the down-bending Type II galaxies the star formation process does not change drastically at the break in either spirals or dwarfs, although a larger sample of spirals would be necessary to make this statement stronger.

In Figure 16 we show a histogram of the ratio of the radius of the furthest out FUV

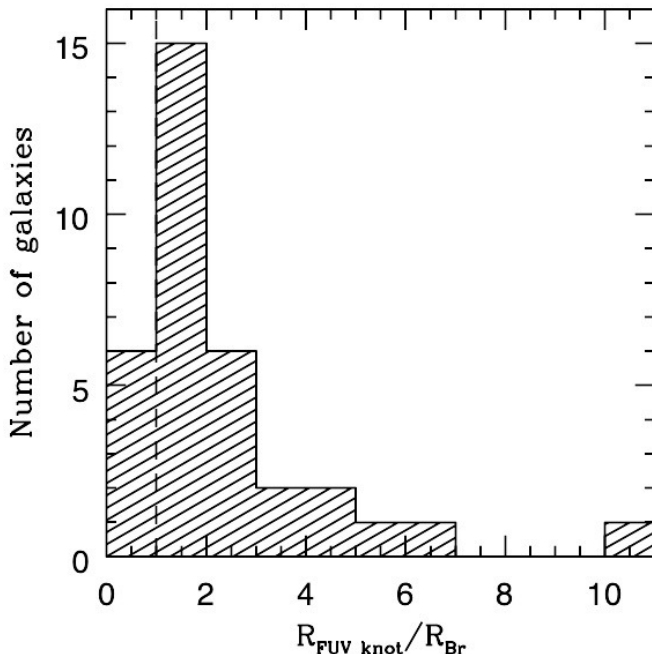


Fig. 16.— Number of galaxies with the given ratio of the radius of the furthest out FUV knot R_{FUVknot} to R_{Br} . The vertical dashed line indicates $R_{\text{FUVknot}}=R_{\text{Br}}$.

knot R_{FUVknot} to R_{Br} . The median value of the sample is 1.8, so the furthest out FUV knot is beyond R_{Br} in most galaxies.

5.4. Gas surface density

Schaye (2004) argues that star formation occurs where there is cold gas that is susceptible to gravitational instabilities, although the connection between cold H I and star formation has been observationally complex in dIrr (e.g. Young & Lo 1996; Young et al. 2003; Begum et al. 2006; de Blok & Walter 2006). The threshold gas column density for this transition has been argued to be about $3\text{-}10 \times 10^{20} \text{cm}^{-2}$ ($2.4\text{-}8 M_{\odot} \text{pc}^{-2}$). Hunter et al. (2016) found that the furthest out FUV knot in the LITTLE THINGS dIrrs were found above a column density of $2 M_{\odot} \text{pc}^{-2}$. The break, according to Schaye, occurs where the average gas density drops below this threshold. In Figure 17 we plot the number of galaxies with a given H I surface density at R_{Br} . We see that most galaxies have values between 1.6 and $10 M_{\odot} \text{pc}^{-2}$. Although these values are consistent with various suggestions on density thresholds, this is a very broad range of values, implying that a single gas density threshold is too simple to explain R_{Br} .

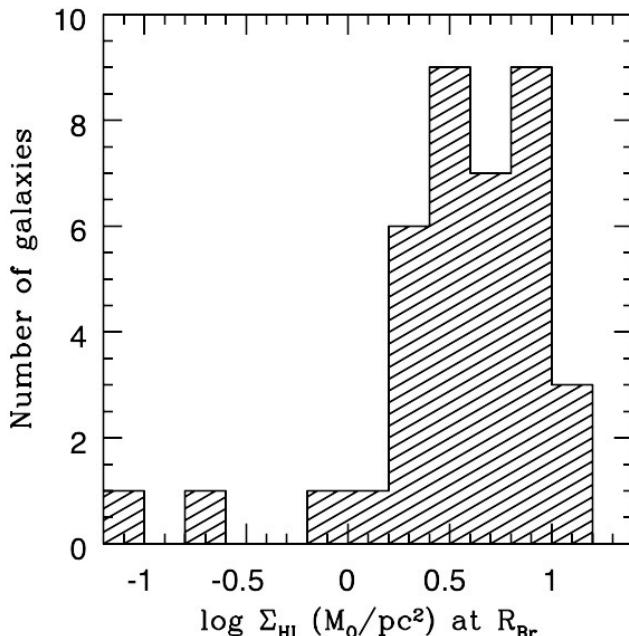


Fig. 17.— Number of dIrr galaxies with the indicated HI surface density at R_{Br} .

5.5. Stellar disk

Li et al. (2005) found from hydrodynamic simulations that there should be a sharp drop in the SFR at $2R_{\text{D}}$. They suggest that stars are more important than gas in destabilizing dwarf disks, although it is not clear if this means the actions of the stars or the stellar densities play a key role. In Figure 18 we plot a histogram of the ratio $R_{\text{Br}}/R_{\text{D}}$ for the LITTLE THINGS galaxies. We see that the break radius in most (82%) of these galaxies does occur at $0.5-2R_{\text{D}}$. Furthermore, Herrmann et al. (2016) shows that R_{Br} is found at a stellar mass surface density of $1-2 M_{\odot} \text{ pc}^{-2}$ for Type II dIrrs, although higher mass surface densities for BCDs. Thus, there appears to be a relationship between R_{Br} and the stellar surface density.

5.6. Stellar bar potentials

Some dIrr galaxies are barred as evidenced by the rotation of the optical surface brightness isophotes with increasing radius. In one case, we also observe streaming motions of the HI around the bar (Hunter et al. 2019b). There are 12 LITTLE THINGS dIrrs for which there is evidence for a bar (Hunter & Elmegreen 2006), and we use these to explore the impact of a bar potential on R_{Br} . For these galaxies we have determined the distance of the end of the bar in the plane of the galaxy. Since most bars are offset from the galactic center, we have found the furthest point of the bar from the center of the galaxy. This information

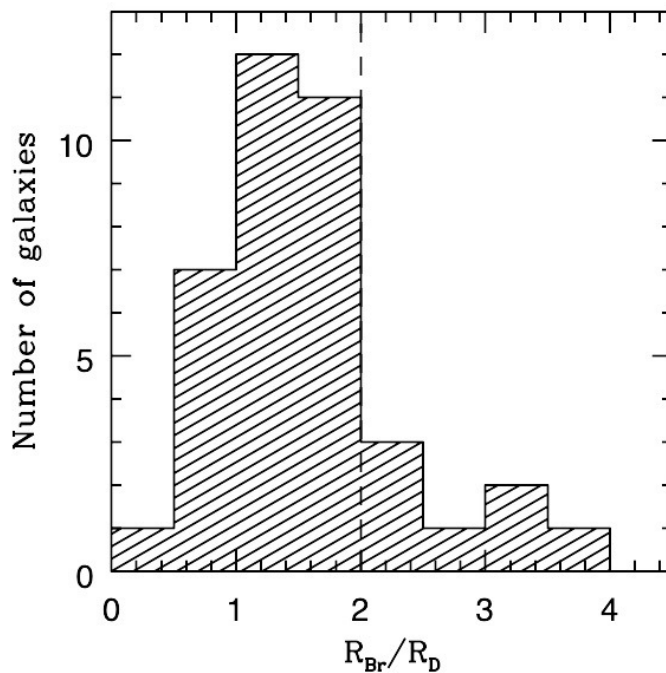


Fig. 18.— Number of dIrr galaxies with the indicated R_{Br} in units of R_{D} . The vertical dashed line marks $R_{\text{Br}}=2R_{\text{D}}$.

is given in Table 7. R_{Bar} is the semi-major axis of the bar and $R_{\text{Bar end}}$ is the largest distance of the edge of the bar from the center of the galaxy. R_{Br} is plotted against $R_{\text{Bar end}}$ in Figure 19. We see that $R_{\text{Br}} \sim R_{\text{Bar end}}$, which could imply a connection between the bar and the profile break in these galaxies. However, not all dIrr with breaks have bars.

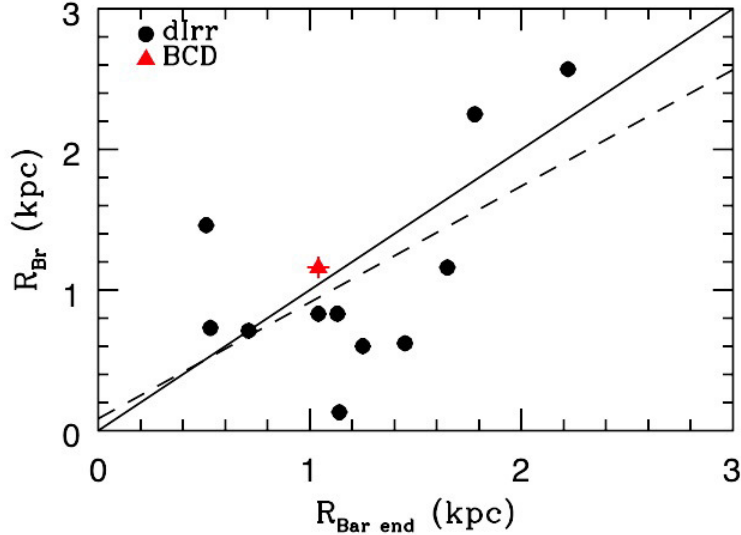


Fig. 19.— Largest distance of the end of the bar from the center of the galaxy $R_{\text{Bar end}}$ vs. R_{Br} for the LITTLE THINGS galaxies with bars (Hunter & Elmegreen 2006). The slanted solid line denotes a one-to-one relationship. Errorbars are plotted but are generally smaller than the point size. The dashed line is a fit to the points, with correlation coefficient of 0.6 and standard deviation of 0.6: $R_{\text{Br}} = (0.086 \pm 0.46) + (0.83 \pm 0.35)R_{\text{Bar end}}$.

Table 7. Stellar bar structures

Galaxy	R_{Bar} (arcsec)	$R_{\text{Bar end}}$ (kpc)	$R_{\text{Br}}/R_{\text{Bar end}}$
DDO 43	13.5 ± 0.7	0.51 ± 0.03	2.9 ± 0.16
DDO 70	102.9 ± 5.1	1.14 ± 0.03	0.1 ± 0.01
DDO 126	35.9 ± 1.8	1.25 ± 0.04	0.5 ± 0.03
DDO 133	83.9 ± 4.2	1.78 ± 0.07	1.3 ± 0.07
DDO 154	54.3 ± 2.7	1.45 ± 0.05	0.4 ± 0.03
F564-V3	11.4 ± 0.6	0.53 ± 0.02	1.4 ± 0.09
NGC 2366	119.3 ± 6.0	2.22 ± 0.10	1.2 ± 0.05
NGC 3738	64.8 ± 3.2	1.65 ± 0.08	0.7 ± 0.03
NGC 4163	45.6 ± 2.3	0.71 ± 0.03	1.0 ± 0.06
NGC 4214	53.9 ± 2.7	1.04 ± 0.04	0.8 ± 0.03
WLM	203.1 ± 10.1	1.13 ± 0.05	0.7 ± 0.04
Haro 36	17.7 ± 0.9	1.12 ± 0.04	1.0 ± 0.04

6. Summary

We have examined the relationship between properties of the stellar disk, the gas disk, and young stars in the LITTLE THINGS sample of nearby dIrr galaxies. The stellar disk is characterized by the disk scale length R_D , the radius at which the V -band surface brightness profile changes slope R_{Br} , and a measure of the central concentration of the stellar mass C_{31} . The H I surface density radial profile is fit with a Sersic function with parameters of extrapolated central surface gas density $\log \Sigma_{HI}^0$, characteristic radius $R_{0,HI}$, and curvature of the profile n_{HI} . The FUV surface brightness profile is fit with three similar parameters: $\log \mu_{FUV}^0$, $R_{0,FUV}$, n_{FUV} .

We include the ratio of the radius that contains 50% of the H I to the radius that contains 90% of the total H I. The rotation curve is fit with a function that includes the asymptotic velocity V_c , the radius where the rotation speed levels off or increases more slowly R_t , and the sharpness of the transition γ . FUV images are used as tracers of young stars, and we specifically look at the ratio of young to older stars interior and exterior to R_{Br} . We include 5 spiral galaxies in this examination for comparison. We also consider the radial extent of H α emission $R_{H\alpha}$, the radial extent of knots of FUV emission $R_{FUVknot}$, the ratio of FUV emission within one disk scale length to that in an annulus from 1 to 3 R_D as a measure of the concentration of the star formation activity, and the galactic SFR determined from the integrated FUV emission. We also compare our data to predictions for what happens at R_{Br} , including the gas and stellar mass surface densities and R_D .

Comparing the H I disk with the stellar disk, we find the following:

(1) Most of our dIrrs have H I surface density profiles that fall off with radius with smaller n_{HI} than that of an exponential disk. This means that the H I profile is flatter in the center before falling off more precipitously compared to an $n = 1$ exponential disk profile that falls off steadily from the center.

(2) Those galaxies closer to $n_{HI} = 1$ have, relative to $R_{0,HI}$, larger $R_{H\alpha}$, R_D , and R_{50} . R_0/R_{50} and R_{50}/R_{90} are related to n_{HI} as expected for a Sersic profile.

(3) The integrated SFR increases with extrapolated central H I surface density.

(4) There is no correlation between the H I surface density shape defined by n_{HI} and the degree of central concentration of the stellar mass, but the young stars are more centrally concentrated in galaxies with a more steady fall off of gas density from the center (larger n_{HI}).

Looking at R_{Br} , we find the following:

(1) The break radius R_{Br} is generally smaller than the characteristic radius of the H I profile $R_{0,\text{HI}}$, is found at $0.5\text{-}2R_{\text{D}}$, and is roughly near the transition radius of the H I rotation curve R_t .

(2) For dIrr galaxies with down-bending surface brightness profiles, the ratio of the SFR before R_{Br} to that after the break, normalized to the starlight from older stars in the same area, is about one. That is, the star formation activity does not change drastically at the break. A small sample of spirals have similar ratios, suggesting that this applies to spirals as well.

(3) There is a tighter relationship between R_{Br} and the stellar disk than with the H I disk.

Considering the fall-off of H I in the inner regions as indicated by a low Sersic index, n_{HI} , we suggest the following interpretation:

(1) The observed increase in H I scale length with decreasing index n_{HI} fits well to a model where the total gas has a Sersic profile with an index and scale length comparable to that of the stellar disk, and where there is a range for the molecular fraction in the center that extends up to 100%. In this model, the molecular surface density scales with a power of the total gas surface density, consistent with molecular cloud formation at the dynamical rate of the midplane gas. Conversion of H I to invisible molecules then causes the inner fall off in the H I profile that increases the H I scale length and lowers n_{HI} .

(2) The radial profile of the molecular fraction is determined by converting the radial profile of the FUV flux, fitted with a Sersic function, into a radial profile of molecular surface density, using standard calibrations for star formation. The sum of this molecular surface density and the Sersic fit to the H I profile gives the total gas profile, which then gives the molecular fraction. The average molecular fraction in the inner $3R_{\text{D}}$ for all of our galaxies is $23 \pm 17\%$.

A. I. E., H. T., and E. G. appreciate the MIT Department of Earth, Atmospheric, and Planetary Sciences for supporting the MIT Field Camp at Lowell Observatory in 2014, 2017, and 2019 and Dr. Amanda Bosh for organizing and running that program. B. B. is grateful for funding from the NAU Space Grant program in 2015 and Kathleen Stigmon for running that. D. A. H. appreciates assistance for publication provided by the National Science Foundation grant AST-1907492. S.-H. O. acknowledges support from National Research Foundation of Korea (NRF) grant NRF-2020R1A2C1008706 funded by the Korean government Ministry of Science and ICT (MSIT). We appreciate thoughtful and detailed suggestions from an anonymous referee that helped improve the manuscript. Lowell Observatory sits at the base

of mountains sacred to tribes throughout the region. We honor their past, present, and future generations, who have lived here for millennia and will forever call this place home.

Facilities: VLA GALEX

A. Spiral Surface Photometry

UBVJHK and $H\alpha$ surface photometry for the LITTLE THINGS dIrr galaxies was presented originally by Hunter & Elmegreen (2004) and Hunter & Elmegreen (2006), and other passbands were added as they became available, for example FUV and NUV by Hunter et al. (2010) and *Spitzer* 3.6 and 4.5 micron by Zhang et al. (2012). These azimuthally-averaged profiles were analyzed for breaks by Herrmann et al. (2013). Measuring the surface photometry on the *V* and FUV images of spirals followed the same process as for the dwarfs with the following exceptions: 1) there was no nuclear region in the dIrrs that needed to be subtracted from the profile, and 2) the reddening correction in the dIrrs was a simple constant and not a function of radius. In addition, the process of fitting the profiles and determining the number and location of breaks in the profiles in the dwarfs was more sophisticated than what we did for the spiral galaxies here. There we were fitting 11 passbands in 141 galaxies and so doing this entirely by hand was not feasible. So Herrmann et al. (2013) wrote an iterative program to determine the best fit and whether there was a single or double exponential, but some human intervention was required so we referred to this as “human-assisted computer break fitting.” See Herrmann et al. (2013) for the details. For the spiral galaxies, the break was determined by eye and a linear fitting algorithm was used for each piece of the profile. The various tables in this paper will be available in machine readable form when the paper is published.

Note: The radius R in surface photometry profiles refers to the semi-major axis at the mid-point of the annulus in which the surface brightness or surface mass density was measured.

Here we describe the reduction of the spiral galaxy imaging data. The spiral sample was chosen to be representative of morphological type Sa, Sb, Sc, and Sd, to not be too edge on, to be observable by us, to have FUV imaging in the NGS catalog, and to have a break in the *V*-band surface brightness profile. The sample size was limited by our time, but it gives a suggestion of how spirals might compare to dIrr galaxies in terms of what happens to the star formation at the *V*-band break. We co-added the *V*-band images, removed foreground and background objects, and fit and subtracted the sky. We fit an outer contour with an ellipse to determine the center of the galaxy, position angle P.A., and minor-to-major axis

ratio b/a . These parameters were held fixed as we measured the V -band and FUV flux in ellipses of increasing major axis. From this we determined the surface brightness in annuli.

We applied a correction for foreground reddening $E(B-V)_f$ using $A_V = E(B-V)_f \times 3.1$ and $A_{FUV} = E(B-V)_f \times 8.24$. We corrected for internal extinction $E(B-V)_i$ using the procedure outlined by Hunter et al. (2013). We use the $H\alpha$ extinction as a function of radius from Prescott et al. (2007), the ratio of the $H\alpha$ extinction to the reddening from Calzetti et al. (2000), and the relationship of the $H\alpha$ extinction to the extinction of stars from Calzetti (1997).

We identified the break in the V -band surface brightness profile, and fit the profile interior and exterior to R_{Br} with a straight line. We used the extinction corrected photometry to determine the total FUV and V -band flux interior and exterior to R_{Br} . We then subtracted the V -band flux of the nucleus from the integrated interior V flux by extrapolating the interior exponential disk inward.

The V and FUV surface brightness profiles and the exponential fits are shown in Figures 20 to 24. The galaxies and their properties are given in Tables 8, 9, and 10.

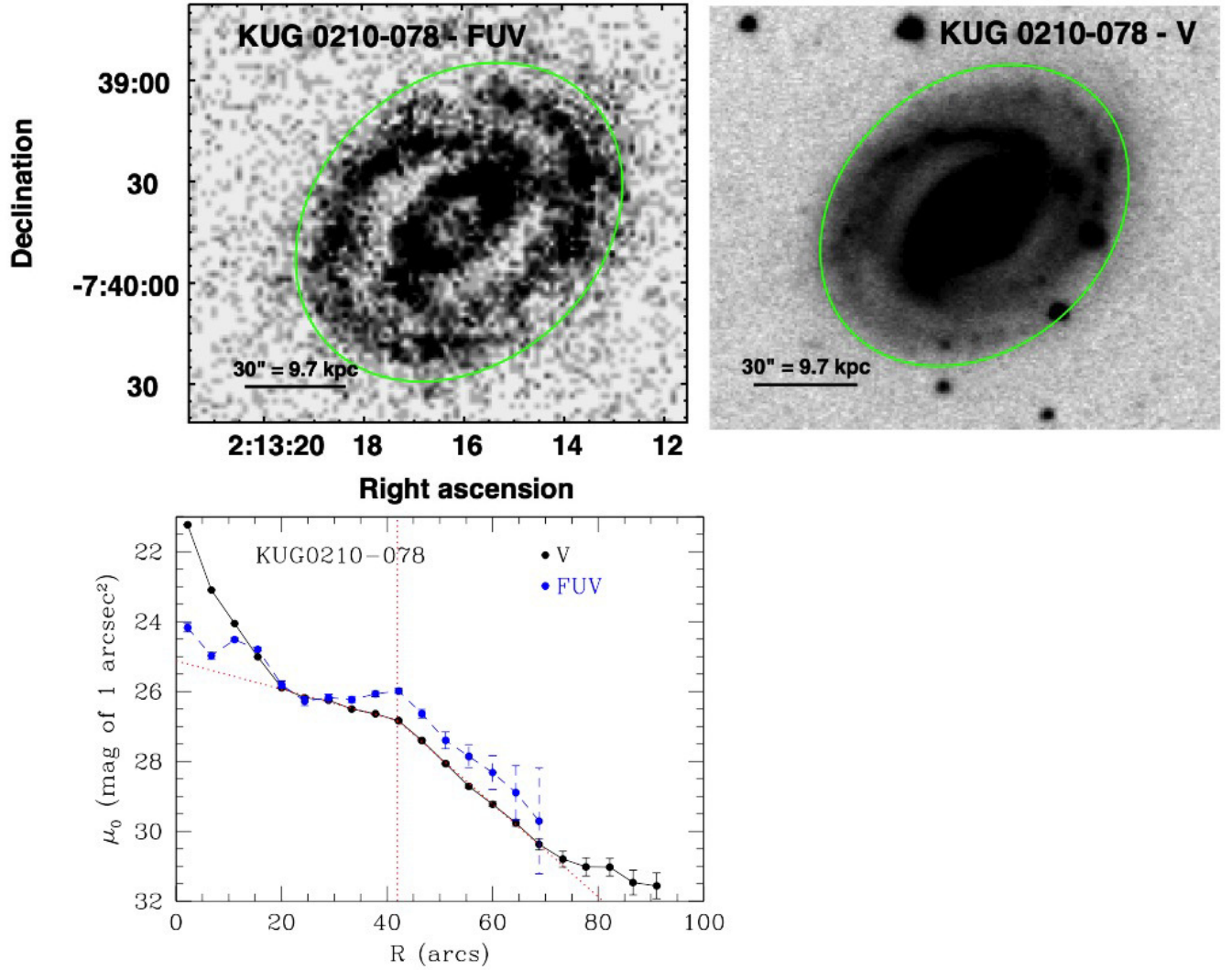


Fig. 20.— *Top*: FUV and *V*-band images of KUG 0210-078. The green ellipse is the 11th ellipse in the surface photometry and shows the centering and P.A. of the ellipses. *Bottom*: FUV and *V*-band surface photometry corrected for foreground and internal extinction. The vertical red dotted line marks the break radius. The slanted dotted red lines are the fits to the surface photometry.

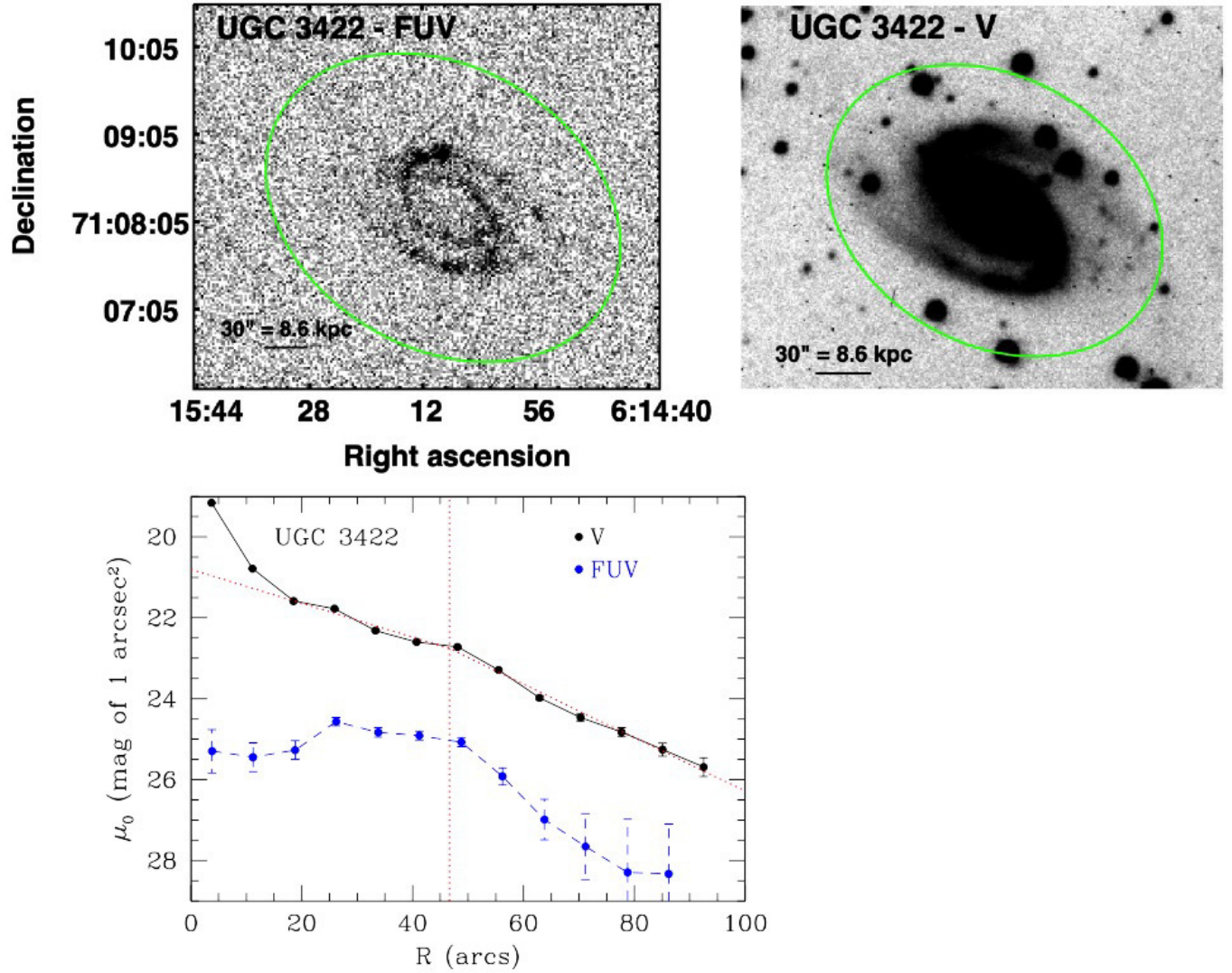


Fig. 21.— *Top*: FUV and *V*-band images of UGC 3422. The green ellipse is the 13th ellipse in the surface photometry and shows the centering and P.A. of the ellipses. *Bottom*: FUV and *V*-band surface photometry corrected for foreground and internal extinction. The vertical red dotted line marks the break radius. The slanted dotted red lines are the fits to the surface photometry.

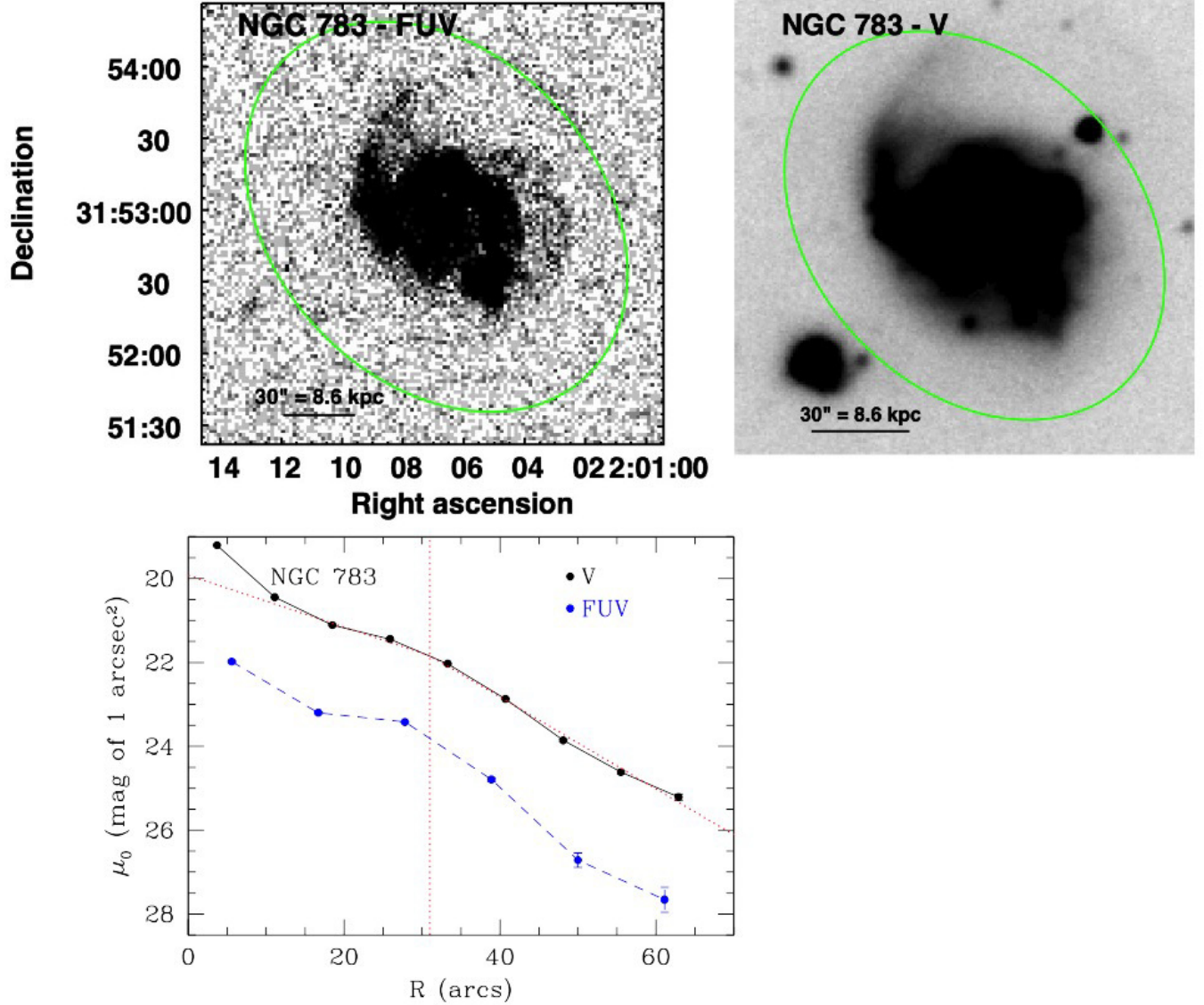


Fig. 22.— *Top*: FUV and *V*-band images of NGC 783. The green ellipse is the 6th ellipse in the surface photometry of the FUV image and the 9th ellipse in the *V*-band surface photometry, and shows the centering and P.A. of the ellipses. *Bottom*: FUV and *V*-band surface photometry corrected for foreground and internal extinction. The vertical red dotted line marks the break radius. The slanted dotted red lines are the fits to the surface photometry.

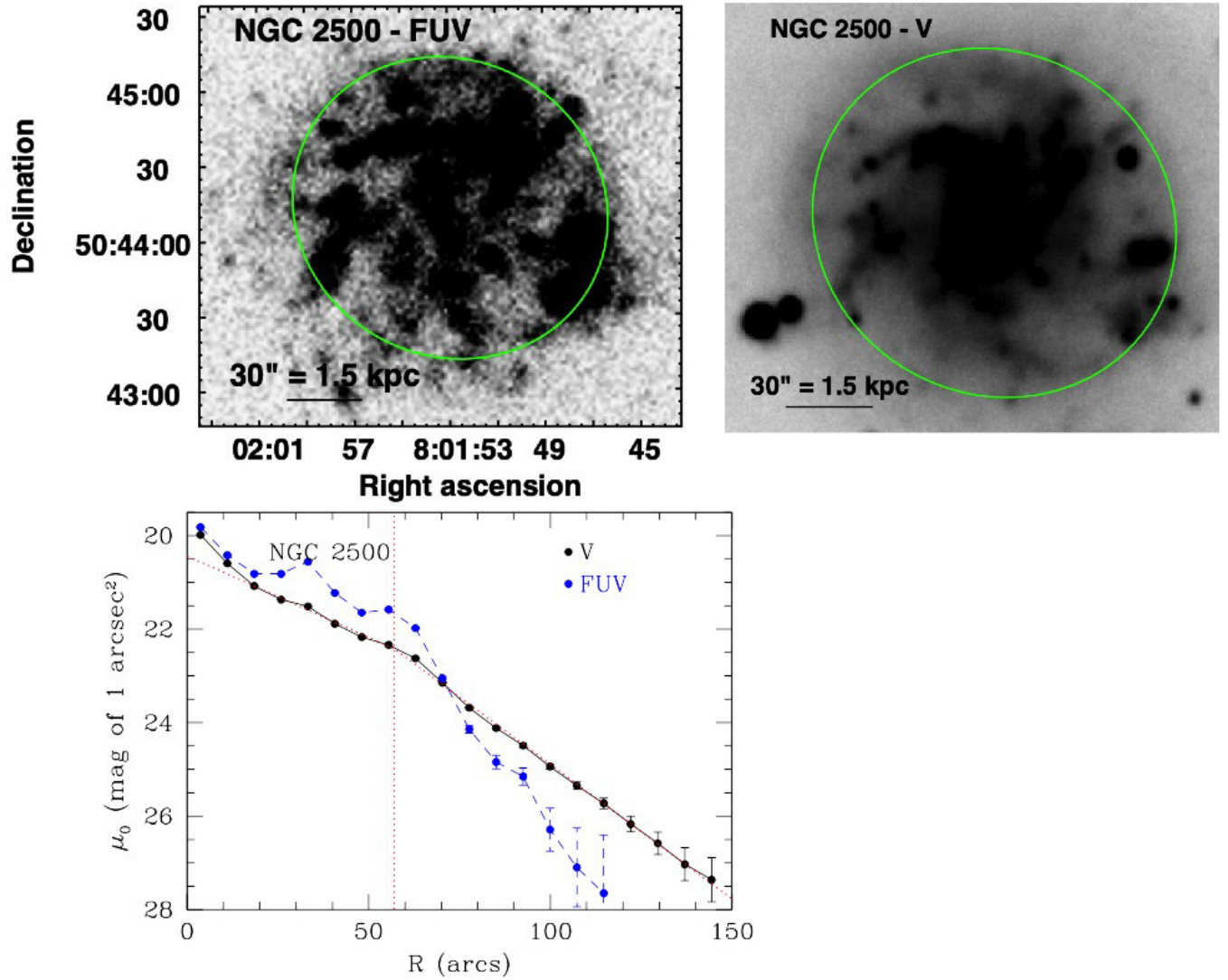


Fig. 23.— *Top:* FUV and *V*-band images of NGC 2500. The green ellipse is the 9th ellipse in the surface photometry and shows the centering and P.A. of the ellipses. *Bottom:* FUV and *V*-band surface photometry corrected for foreground and internal extinction. The vertical red dotted line marks the break radius. The slanted dotted red lines are the fits to the surface photometry.

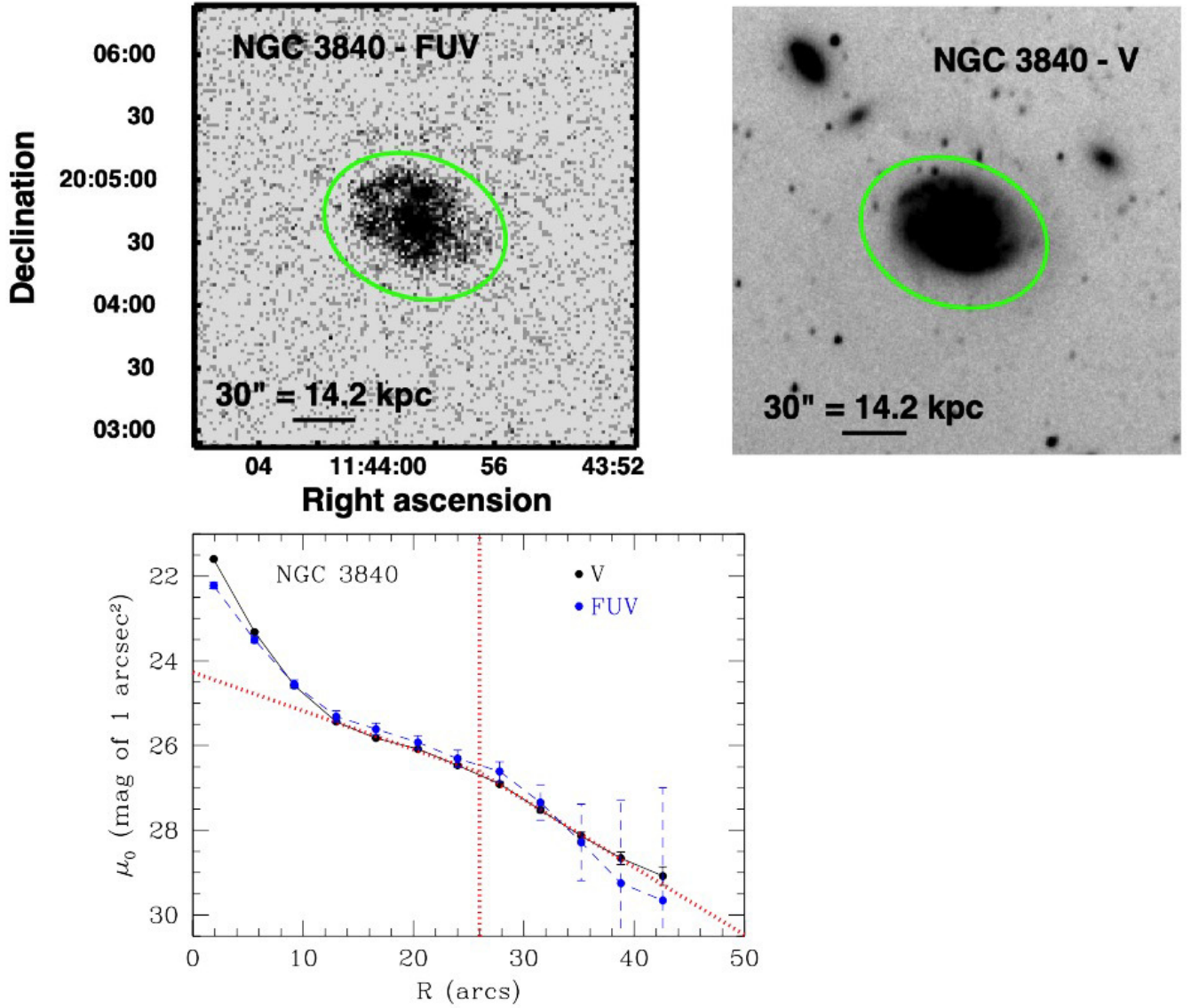


Fig. 24.— *Top*: FUV and *V*-band images of NGC 3840. The green ellipse is the 12th ellipse in the surface photometry and shows the centering and P.A. of the ellipses. *Bottom*: FUV and *V*-band surface photometry corrected for foreground and internal extinction. The vertical red dotted line marks the break radius. The slanted dotted red lines are the fits to the surface photometry.

Table 8. Spirals included in the FUV study

Galaxy	Type	D(Mpc) ^a	Ref for D	M_V	$E(B - V)_f^b$	R_{Br} (arcs) ^c	R_D (arcs) ^d
KUG 0210-078	Sa	66.9±4.7	NED	-18.10 ± 0.15	0.024	41.9 ± 2.3	26.5 ± 1.9
NGC 3840	Sa	97.5±3.1	1	-18.45 ± 0.07	0.019	26.0 ± 3.3	14.5 ± 1.1
UGC 3422	Sb	58.8±9.9	2	-21.34 ± 0.37	0.174	46.7 ± 16.4	25.9 ± 3.1
NGC 783	Sc	59.4±5.2	3	-21.27 ± 0.19	0.054	31.0 ± 3.6	17.5 ± 2.8
NGC 2500	Sd	10.1±1.4	4	-18.19 ± 0.30	0.036	57.0 ± 5.8	31.0 ± 0.9

^aDistance to the galaxy. We used a SNIa, SNII, or Tully-Fisher derived distance, when available. Uncertainty in the distance is folded into the uncertainty of M_V .

^bForeground Milky Way reddenings $E(B - V)_f$ are taken from NED (Schlafly & Finkbeiner 2011).

^cBreak radius at which the V -band surface brightness profile changes slope.

^dDisk scale length measured from the V -band surface brightness profile.

References. — (1) Springob et al. (2009); (2) Theureau et al. (2007); (3) Ganeshalingam et al. (2013); (4) Tully & Fisher (1988)

Table 9. Spiral Imaging Photometry

Galaxy	V Obs (No. exposures × exposure time (s))	FUV exp time (s)	Center RA, Decl. h:m:s, d:m:s	P.A. (deg)	b/a	Interior ^a		Exterior ^a	
						μ_{cen}	b	μ_{cen}	b
KUG 0210-078	10 × 600	1680	2:13:15.7, -7:39:42	-48	0.79	25.1 ± 0.1	0.041 ± 0.003	21.3 ± 0.1	0.133 ± 0.002
NGC 3840	13 × 600	942	11:43:59.0, 20:04:38	70	0.76	24.7 ± 0.1	0.075 ± 0.006	22.6 ± 0.1	0.158 ± 0.003
UGC 3422	9 × 600	1661	6:15:09.1, 71:08:12	60	0.75	20.8 ± 0.2	0.042 ± 0.005	19.7 ± 0.2	0.066 ± 0.003
NGC 783	6 × 600	1972	2:01:06.6, 31:52:57	43	0.75	19.9 ± 0.3	0.062 ± 0.010	18.4 ± 0.3	0.110 ± 0.005
NGC 2500	7 × 600	2974	8:01:52.7, 50:44:13	60	0.92	20.4 ± 0.1	0.035 ± 0.001	19.1 ± 0.1	0.057 ± 0.001

^aFits to $\mu_{V,0} = \mu_{\text{cen}} + bR(\text{arcs})$ interior and exterior to R_{Br} .

Table 10. FUV interior and exterior to R_{Br}

Galaxy	Break Type ^a	log Interior/Exterior ^b	
		FUV/Area	FUV/V
KUG 0210-078	II	0.43 ± 0.06	-0.09 ± 0.01
NGC 3840	II	0.49 ± 0.17	0.13 ± 0.01
UGC 3422	II	0.18 ± 0.38	-0.12 ± 0.02
NGC 783	II	0.64 ± 0.11	-0.06 ± 0.01
NGC 2500	II	0.73 ± 0.09	0.14 ± 0.00

^aType of surface brightness profile break in the V -band. "II" refers to a downward break, and "III" to an upward bend.

^bThe FUV flux is normalized by the area over which it is measured, "FUV/Area," or by the V -band flux measured over the same area, "FUV/ V ." The ratio that is given is FUV/Area or FUV/ V measured interior to the surface brightness profile break to that measured exterior to the break.

REFERENCES

- Andersen, R.-P., & Burkert, A. 2000, *ApJ*, 531, 296
- Bakos, J., Trujillo, I., & Pohlen, M. 2008, *ApJ*, 683, L103
- Barnes, K., van Zee, L., Côté, S., & Schade, D. 2012, *ApJ*, 757, id 64
- Begum, A., Chengalur, J. N., Karachentsev, I. D., Kaisin, S. S., & Sharina, M. E. 2006, *MNRAS*, 365, 1220
- Bellazzini, M., Beccari, G., Fraternali, F., et al. 2014, *Å*, 566, 44
- Bigiel, F., Leroy, A., Walter, F., et al. 2008, *AJ*, 136, 2846
- Bigiel, F., Leroy, A., Walter, F., et al. 2010, *AJ*, 140, 1194
- Bolatto, A. D., Leroy, A. K., Jameson, K., et al. 2011, *ApJ*, 741, 12
- Bournaud, F., Elmegreen, B. G., & Elmegreen, D. M. 2007, *ApJ*, 670, 237
- Broeils, A. 1992, PhD Thesis, Univ. Groningen
- Calzetti, D. 1997, in *AIP Conf. Proc.* 408, *The Ultraviolet Universe at Low and High Redshift: Probing the Progress of Galaxy Evolution*, ed. W. H. Waller, M. N. Fanelli, J. E. Hollis, & A. C. Danks (Woodbury, MN: AIP), 403
- Calzetti, D., Armus, L., Bohlin, R. C., et al. 2000, *ApJ*, 533, 682
- Chabrier, G. 2003, *PASP*, 115, 763
- Courteau, S. 1997, *AJ*, 114, 2402
- de Blok, W. J. G., & Walter, F. 2006, *AJ*, 131, 363
- Deharveng, J. M., Sasseen, T. P., Buat, V., et al. 1994, *A&A*, 289, 715
- de Vaucouleurs, G. 1977, *Evolution of galaxies and stellar populations*, ed. R. B. Larson, & B. M. Tinsley, Yale Univ. Obs., New Haven, 43
- de Vaucouleurs, G., & Capaccioli, M. 1979, *ApJS*, 40, 699
- El-Badry, K., Wetzell, A., Geha, M., Hopkins, P., Kereš, D., Chan, T., & Faucher-Giguère, C.-A. 2016, *ApJ*, 820, 131
- Elmegreen, B. G., & Hunter, D. A. 2015a, *ApJ*, 805, id 145

- Elmegreen, B. G. 2015b, *ApJL*, 814, L30
- Elmegreen, B. G. 2018, *ApJ*, 854, 16
- Elmegreen, B. G. & Elmegreen, D.M. 2020, *ApJ*, 895, 71
- Erwin, P., Beckman, J. E., & Pohlen, M. 2005, *ApJ*, 626, L81
- Freeman, K. C. 1970, *ApJ*, 160, 811
- Gallart, C., Stetson, P. B., Meschin, I. P., Pont, F., & Hardy, E. 2008, *ApJ*, 682, L89
- Ganeshalingam, M., Li, W., & Filippenko, A. V., 2013, *MNRAS*, 433, 244
- Gil de Paz, A., Boissier, S., Madore, B. F., Seibert, M., Joe, Y., et al. 2007, *ApJS*, 173, 185
- Goldreich, P., & Lynden-Bell, D. 1965, *MNRAS*, 130, 97
- Governato, F., Zolotov, A., Pontzen, A., Christensen, C., Oh, S. H., Brooks, A. M., Quinn, T., Shen, S., & Wadsley, J. 2012, *MNRAS*, 422, 1231
- Herrmann, K. A., Hunter, D. A., & Elmegreen, B. G. 2013, *AJ*, 146, 104
- Herrmann, K. A., Hunter, D. A., & Elmegreen, B. G. 2016, *AJ*, 151, 145
- Hunter, D. A. 2008, “Dust and Gas as Seeds for Metal-Poor Star Formation,” in *Low Metallicity Star Formation: From the First Stars to Dwarf Galaxies, Proceedings of IAU Symposium No. 255*, eds. L. K. Hunt, S. Madden & R. Schneider (Cambridge: Cambridge Univ Press), p 226
- Hunter, D. A., & Elmegreen, B. G. 2004, *AJ*, 128, 2170
- Hunter, D. A., & Elmegreen, B. G. 2006, *ApJS*, 162, 49
- Hunter, D. A., Elmegreen, B. G., & Baker, A. L. 1998, *ApJ*, 493, 595
- Hunter, D. A., Elmegreen, B. G., & Gehret, E. 2016, *AJ*, 151, 136
- Hunter, D. A., Elmegreen, B. G. & Ludka, B. C. 2010, *AJ*, 139, 447
- Hunter, D. A., Elmegreen, B. G., Oh, S.-H., et al. 2011, *AJ*, 142, 121
- Hunter, D. A., Elmegreen, B. G., Rubin, V. C., & Ashburn, A. 2013, *AJ*, 146, 92
- Hunter, D. A., Ficut-Vicas, D., Ashley, T., et al. 2012, *AJ*, 144, id 134

- Hunter, D. A., Elmegreen, B. G., & Berger, C. L. 2019a, *AJ*, 157, 241
- Hunter, D. A., & Gallagher, J. S. 1985, *AJ*, 90, 1789
- Hunter, D. A., Laufman, L., Oh, S.-H., Levine, S. E., & Simpson, C. E. 2019b, *AJ*, 158, 23
- Kenney, J. D., & Young, J. S. 1988, *ApJ*, 326, 588
- Kennicutt, R. C., Jr. 1989, *ApJ*, 344, 685
- Kennicutt, R. C., Jr. 1998, *ARAA*, 36, 189
- Leroy, A. K., Bolatto, A., Walter, F., & Blitz, L. 2006 *ApJ*, 643, 825
- Leroy, A. K., Walter, F., Brinks, E., et al. 2008, *AJ*, 136, 2782
- Li, Y., Mac Low, M.-M., & Klessen, R. S. 2005, *ApJ*, 626, 823
- Martin, D. C., Fanson, J., Schiminovich, D., et al. 2005, *ApJ*, 619, L1
- Meschin, I., Gallart, C., Aparicio, A., Hidalgo, S. L., Monelli, M., Stetson, P. B., & Carrera, R. 2014, *MNRAS*, 438, 1067
- Meurer, G. R., Carignan, C., Beaulieu, S. F., & Freeman, K. C. 1996, *AJ*, 111, 1551
- Oh, S.-H., Hunter, D., Brinks, E., Elmegreen, B., Schrubba, A., et al. 2015, *AJ*, 149, id 180
- Ohta, K., Sasaki, M., & Saito, M. 1988, *PASJ*, 40, 653
- Ohta, K., Sasaki, M., Yamada, T., Saito, M., & Nakai, N. 1992, *PASJ*, 44, 585
- Pan, Z., Li, J., Lin, W., Wang, J., Fan, L., & Kong, X. 2015, *ApJ*, 804, L42
- Prescott, M. K. M., Kennicutt, R. C., Jr., Bendo, G. J., et al. 2007, *ApJ*, 668, 182
- Rao, S., & Briggs, F. 1993, *ApJ*, 419, 515
- Rubio, M., Elmegreen, B. G., Hunter, D. A., et al. 2015, *Nature*, 525, 218
- Roškar, R., Debattista, V. P., Stinson, G. S., Quinn, T. R., Kaufmann, T., & Wadsley, J. 2008, *ApJ*, 675, 65
- Rownd, B. K., & Young, J. S. 1999, *AJ*, 118, 670
- Saha, A., Olszewski, E. W., Brondel, B., et al. 2010, *AJ*, 140, 1719
- Sanna, N., Bono, G., Stetson, P. B., et al. 2010, *ApJ*, 722, L244

- Schaye, J. 2004, ApJ, 609, 667
- Schlafly, E. F., & Finkbeiner, D. P. 2011, ApJ, 737, 103
- Sersic, J. L. 1982, Extragalactic Astronomy, Geophysics and Astrophysics Monographs, Lecture notes from Cordoba (Dordrecht: Reidel)
- Simpson, C. E., & Gottesman, S. T. 2000, AJ, 120, 2975
- Springob, C.M., Masters, K.L., Haynes, M. P., Giovanelli, R., & Marinoni, C. 2009, ApJS, 182, 474
- Struck, C., & Elmegreen, B. G. 2017, MNRAS, 469, 1157
- Taylor, C. L., Hüttemeister, S., Klein, U., & Greve, A. 1999, A&A, 349, 424
- Theureau, G., Hanski, M., Coudreau, N. Hallet, N., & Martin, J.-M., 2007, A&A, 465, 71
- Thilker, D. A., Bianchi, L., Boissier, S., et al. 2005, ApJ, 619, L79
- Toomre, A. 1964, ApJ, 139, 1217
- Tully, R. B., & Fisher, J. R. 1988, Catalog of Nearby Galaxies, Cambridge University Press
- van der Hulst, J. M., Skillman, E. D., Smith, T. R., et al. 1993, AJ, 106, 548
- van Zee, L., Skillman, E. D., & Salzer, J. J. 1998, AJ, 116, 1186
- Wang, J., Fu, J., Aumer, M., et al. 2014, MNRAS, 441, 2159
- Warmels, R. H. 1986, PhD Thesis, Univ. Groningen
- Watkins, A. E., Laine, J., Comerón, S., et al. 2019, *a*, 625, 36
- Williams, B. F., Dalcanton, J. J., Dolphin, A. E., Holtzman, J., & Sarajedini, A. 2009, ApJ, 695, L15
- Wilson, C. D., & Reid, I. N. 1991, ApJ, 366, L11
- Wilson, C.D., Elmegreen, B.G., Bemis, A. & Brunetti, N. 2019, ApJ, 882,5
- Young, L. M., & Lo, K. Y. 1996, ApJ, 462, 203
- Young, L. M., van Zee, L., Lo, K. Y., Dohm-Palmer, R. C., & Beierle, M. 2003, ApJ, 592, 111

Zhang, H.-X., Hunter, D. A., Elmegreen, B. G., Gao, Y., & Schruba, A. 2012, *AJ*, 143, 47